

**UNITED STATES AIR FORCE
RESEARCH LABORATORY**

**A Model of the Acoustic Intensity Field
Generated by a Multi-Engine
Turbo-Prop Aircraft**

Brian Scott Davis

September 2002

Final Report for the Period June 2001 to September 2002

20030401 011

Approved for public release; distribution is unlimited.

**Human Effectiveness Directorate
Crew System Interface Division
2610 Seventh Street
Wright-Patterson AFB OH 45433-7901**

NOTICES

When US Government drawings, specifications, or other data are used for any purpose other than a definitely related Government procurement operation, the Government thereby incurs no responsibility nor any obligation whatsoever, and the fact that the Government may have formulated, furnished, or in any way supplied the said drawings, specifications, or other data, is not to be regarded by implication or otherwise, as in any manner licensing the holder or any other person or corporation, or conveying any rights or permission to manufacture, use, or sell any patented invention that may in any way be related thereto.

Please do not request copies of this report from the Air Force Research Laboratory. Additional copies may be purchased from:

National Technical Information Service
5285 Port Royal Road
Springfield, Virginia 22161

Federal Government agencies and their contractors registered with the Defense Technical Information Center should direct requests for copies of this report to:

Defense Technical Information Center
8725 John J. Kingman Road, Suite 0944
Ft. Belvoir, Virginia 22060-6218

DISCLAIMER

This Technical Report is published as received and has not been edited by the Air Force Research Laboratory, Human Effectiveness Directorate.

TECHNICAL REVIEW AND APPROVAL

AFRL-HE-WP-TR-2002-0191

This report has been reviewed by the Office of Public Affairs (PA) and is releasable to the National Technical Information Service (NTIS). At NTIS, it will be available to the general public.

This technical report has been reviewed and is approved for publication.

FOR THE COMMANDER



MARIS M. VIKMANIS

Chief, Crew System Interface Division
Air Force Research Laboratory

REPORT DOCUMENTATION PAGE

Form Approved
OMB No. 0704-0188

Public reporting burden for this collection of information is estimated to average 1 hour per response, including the time for reviewing instructions, searching existing data sources, gathering and maintaining the data needed, and completing and reviewing the collection of information. Send comments regarding this burden estimate or any other aspect of this collection of information, including suggestions for reducing this burden, to Washington Headquarters Services, Directorate for Information Operations and Reports, 1215 Jefferson Davis Highway, Suite 1204, Arlington, VA 22202-4302, and to the Office of Management and Budget, Paperwork Reduction Project (0704-0188), Washington, DC 20503.

1. AGENCY USE ONLY (Leave Blank)			2. REPORT DATE	3. REPORT TYPE AND DATES COVERED
			September 2002	Final - June 2001 to September 2002
4. TITLE AND SUBTITLE			5. FUNDING NUMBERS	
A Model of the Acoustic Intensity Field Generated by a Multi-Engine Turbo-Prop Aircraft			PE - 62202F PR - 7184 TA - 718416 WU - 71841609	
6. AUTHOR(S)			8. PERFORMING ORGANIZATION REPORT NUMBER	
Brian Scott Davis			AFRL-HE-WP-TR-2002-0191	
7. PERFORMING ORGANIZATION NAME(S) AND ADDRESS(ES)			10. SPONSORING/MONITORING AGENCY REPORT NUMBER	
Air Force Research Laboratory, Human Effectiveness Directorate Crew System Interface Division Aural Displays and Bioacoustics Branch Air Force Materiel Command Wright-Patterson Air Force Base, OH 45433-7901				
9. SPONSORING/MONITORING AGENCY NAME(S) AND ADDRESS(ES)			11. SUPPLEMENTARY NOTES	
12a. DISTRIBUTION AVAILABILITY STATEMENT			12b. DISTRIBUTION CODE	
Approved for public release; distribution is unlimited.				
13. ABSTRACT (Maximum 200 words)				
High levels of noise within the fuselage of a turbo-prop aircraft cannot be mitigated by traditional acoustic coating techniques, since the primary frequencies are generally less than 500 Hz. Tests of an advanced device, designed to control the relative phase between the engines, identified 10-20 dB reductions in the acoustic noise levels within the fuselage. An analytical framework was developed to model the observed effects independent of airframe design. The Green's function for the three-dimensional non-homogeneous acoustic wave equation was used to obtain the radiation fields for three specific source functions: a harmonic point source, a pulsating non-harmonic distributed source, and a single uniformly rotating paddle. Comparisons were made between the observed data and models for three specific sets of relative engine phases. Although each model exhibited some of the features of the actual data set, no particular source function reproduced all features of the measured data.				
14. SUBJECT TERMS			15. NUMBER OF PAGES	
acoustics, acoustic modeling, noise, aircraft noise, occupational noise exposure			55	
			16. PRICE CODE	
17. SECURITY CLASSIFICATION OF REPORT		18. SECURITY CLASSIFICATION OF THIS PAGE	19. SECURITY CLASSIFICATION OF ABSTRACT	20. LIMITATION OF ABSTRACT
UNCLASSIFIED		UNCLASSIFIED	UNCLASSIFIED	UL

This page intentionally left blank.

PREFACE

This final report describes the results of work performed to develop a model of noise levels within a multi-engine turbo-prop aircraft. The work was performed from June 2001 to September 2002. The Principal Investigator for this project was Brian Scott Davis of the Air Force Research Laboratory's Aural Displays and Bioacoustics Branch at Wright-Patterson Air Force Base OH. The work was performed under Program Element 62202F, Work Unit 71841609. Robert A. Lee was the project manager.

This page intentionally left blank.

TABLE OF CONTENTS

	Page
Section 1 - INTRODUCTION	1
Section 2 - EXPERIMENTAL	4
Section 3 - THE ANALYTICAL MODEL.....	17
BACKGROUND.....	17
MODEL A (Monochromatic Point Source).....	21
MODEL B (Extended Source Function).....	26
MODEL C (Uniformly Rotating Paddle).....	35
Section 4 - DISCUSSION And CONCLUSIONS.....	43
References.....	46

LIST OF FIGURES

Figure	Page
2.1. C-130 Scale Top View.....	4
2.2. C-130 Scale Frontal View.....	5
2.3. Sampled Microphone Fuselage Locations.....	8
2.4. One/Third Octave Band Spectra at Microphone Seven - Analog Synchrophaser.....	12
2.5. One/Third Octave Band Spectra at Microphone Seven - Digital Synchrophaser.....	12
2.6. Linear Interpolation of the Measured Data - Phase Setting (180°, 180°, 180°, 180°).....	13
2.7. Linear Interpolation of the Measured Data - Phase Setting (150°, 180°, 150°, 120°).....	14
2.8. Linear Interpolation of the Measured Data - Phase Setting (180°, 180°, 150°, 120°).....	15
2.9. Linear Interpolation of the Measured Data - Baseline Analog Controller Configuration.....	16
3.1. Predicted Fuselage Acoustic Intensity - Model A - Phase Angle (180°, 180°, 180°, 180°).....	23
3.2. Predicted Fuselage Acoustic Intensity - Model A - Phase Angle (150°, 180°, 150°, 120°).....	24
3.3. Predicted Fuselage Acoustic Intensity - Model A - Phase Angle (180°, 180°, 150°, 120°).....	25
3.4. Pulsating Disk Propeller Assembly Representation.....	26
3.5. Predicted Fuselage Acoustic Intensity - Model B - Phase Angle (180°, 180°, 180°, 180°).....	32

LIST OF FIGURES (Continued)

3.6. Predicted Fuselage Acoustic Intensity - Model B - Phase Angle (150°, 180°, 150°, 120°).....	33
3.7. Predicted Fuselage Acoustic Intensity - Model B - Phase Angle (180°, 180°, 150°, 120°).....	34
3.8. Predicted Fuselage Acoustic Intensity - Model C - Phase Angle (180°, 180°, 180°, 180°).....	40
3.9. Predicted Fuselage Acoustic Intensity - Model C - Phase Angle (150°, 180°, 150°, 120°).....	41
3.10. Predicted Fuselage Acoustic Intensity - Model C - Phase Angle (180°, 180°, 150°, 120°).....	42

LIST OF TABLES

Table	Page
2.1. Measured Phase Angle Combinations.....	6
2.2. X-Y Coordinates of Microphone Locations.....	9

Section 1 - INTRODUCTION

The C-130 is a four-engine turbo-prop air vehicle principally designed to ferry military payloads in excess of 45,000 pounds.¹ High levels of noise generated by powerful aircraft engines is one of the by-products of being able to airlift heavy military cargo. For example, C-130 flight crew personnel typically experience sound pressure levels (SPL) between 100 and 115 dB, 15-25 dB above the OSHA standard of 90 dB per eight-hour workday.² Intense noise exposures, unfortunately, are not unique experiences and often result in hearing loss for many military personnel. According to data obtained from the Department of Veterans Affairs, the total cost of compensation in 2001 was \$361,362,000 for all veterans having hearing loss identified as a primary disability.³ This permanent impact on human hearing and monetary cost could potentially be mitigated by more widespread application of active noise cancellation techniques.

Active noise cancellation involves creating an equal amplitude but opposite phase waveform to cancel an acoustic source. Area cancellation techniques within an aircraft typically involve coating the walls of the fuselage with lightweight acoustic damping material. Although this approach works well for jet aircraft where a significant amount of the noise generated by the engines is above 500 Hz, it has little effect on turbo-prop aircraft where the spectra is dominated by low frequency tones associated with the blade passage frequency (BPF).^{4,5} Control of these longer wavelengths is generally expensive

and difficult since passive noise control measures require large muffler assemblies or heavy enclosures.^{4,6} Active noise technology provides the solution. The commercial sector has already implemented this technology to minimize the noise generated from air handling system exhaust ducts, automobile engine vibration, and low frequency tonal noise from mid-sized propeller aircraft.⁶

Successful reduction of the acoustic levels within the fuselage of turbo-prop aircraft has been previously demonstrated using two distinct methods. Method One utilizes dedicated sensors positioned in the vicinity of each passenger's head to sample the energy generated by the propellers at the Blade Passage Frequency (BPF) and its harmonics. This data is processed in real time to produce an error signal input to an amplifier/loudspeaker system capable of producing a secondary field which is 180 degrees out of phase with the input. Although effective, installation of multiple amplifier and speaker arrays capable of producing a signal of the required amplitude (100-115 dB) within the fuselage is cost and space prohibitive.^{5, 7, 8}

In an alternative approach, cancellation is accomplished at the source prior to entry into the fuselage by enhanced control of the relative phase between propellers (Method Two).⁹ Microphones are again utilized to develop an error signal that functions as an input to an advanced propeller phase controller, known as a synchrophaser. The synchrophaser couples the error signal with a once per revolution signal of the propeller engine to issue speed and phase control commands to the propeller governor. Propeller

speed and phase are maintained through this method. Phase angles are either commanded manually or automatically via an adaptive search routine.

The purpose of this thesis is to develop an active noise cancellation analytical model (following Method Two) that can accurately predict the acoustic intensity field within the fuselage of a turbo-prop aircraft with respect to the relative propeller phase angle between the four engines. Theoretically, the physical model would enable the development of engines and control systems specifically designed to minimize interior noise independent of airframe design.

Section 2 - EXPERIMENTAL

The test vehicle utilized for these acoustic tests was an operational United States Air Force MC-130E. The C-130 is an all-weather cargo transport specifically tasked to perform infiltration and exfiltration operations in hostile environments. Testing conducted in January 2002 spanned three weeks at Eglin Air Force Base, Florida. During these three weeks, 25 flight hours of data was recorded. Schematic drawings of the aircraft dimensions are provided in Figure 2.1 and Figure 2.2.¹⁰

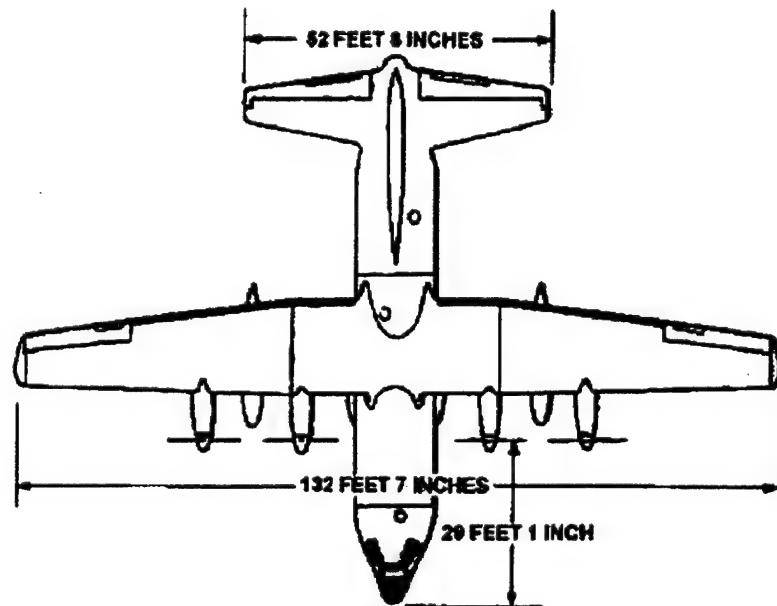


Figure 2.1 C-130 Scale Top View.

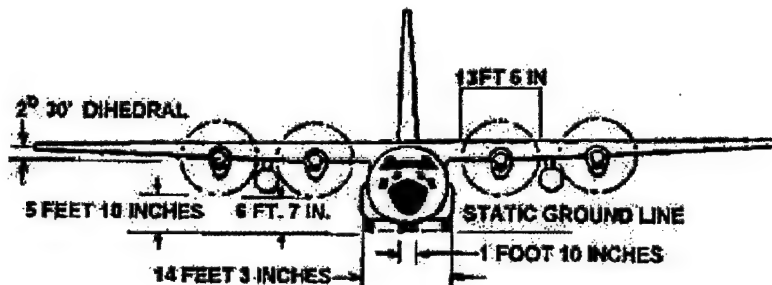


Figure 2.2 C-130 Scale Frontal View. Engines are numbered 1-4 from right to left.

Four Allison turbo-prop engines with an effective shaft horsepower of 4,300 power the aircraft. Each of these turbojet engines drives a four bladed Hamilton Standard propeller assembly that maintains a constant speed of 1020 revolutions per minute (RPM).^{1,10} This corresponds to a primary BPF of 68 Hz and an associated wavelength of 5 meters. Propeller direction is counter clock wise with respect to an observer situated forward of the engines. Engines were identified 1-4, right to left (left to right with respect to the pilot position). Thus in Figure 2.1 and Figure 2.2, engine 2 is the inboard engine to the right of the fuselage. Inter-engine distances of 5 meters for the inboard and 10 meters for the outboard were calculated based upon scale diagrams Figure 2.1 and Figure 2.2. All values are measured with respect to a coordinate system situated at the intersection of the line formed by the propeller hubs and the plane that bisects the fuselage from nose to tail.

Because the C-130 is an aircraft with synchrophased engines, an analog controller has routinely been utilized to maintain a fixed phase relationship between the engines. Either of the two inboard engines can be identified as the master reference. Phase relationships were maintained with respect to the master and changes were accomplished via small perturbations in propeller RPM.¹¹ Since the phase angles were invariant, the analog

system did not compensate for variations in the sound field as a function of aircraft velocity. This resulted in poor management of the interior noise profile.

Engine 1	Engine 2	Engine 3	Engine 4
150	180	120	120
120	180	150	150
150	180	120	150
150	180	150	120
180	180	150	180
120	180	180	150
180	180	150	120
180	180	120	180
180	180	120	120
150	180	150	180
150	180	180	180
150	180	180	150
120	180	180	120
180	180	180	120
120	180	120	150
150	180	180	120
120	180	150	180
180	180	150	150
180	180	180	180
120	180	180	180
150	180	120	180
180	180	180	150
120	180	150	120
120	180	120	180
150	180	150	150
180	180	120	150

Table 2.1 Measured phase angle combinations. Engine #2 was selected as master for all measurements. The phase angle for this engine was arbitrarily set at 180° because the digital controller could not stabilize at zero degrees. Highlighted combinations identify particular combinations for comparison to model results from the next section.

For the acoustic test here, a form-fit function replacement was used (along with the original analog controller), based on an active synchrophaser prototype developed by British Aerospace Electronic (B.A.E.) Systems. In this design, the user maintains the

ability to select a master engine and gains the ability to dial in a particular set of phase angles. These capabilities facilitate better control of the noise signature of the aircraft.

A two-tiered data collection approach was adopted to meet the funding, manpower, and aircraft availability constraints. The first tier consisted of acoustic measurements of both the internal and external sound fields at 27 sets of phase angles. The phase angles measured in tier one are identified in Table 2.1. Engine 2 was designated as the master engine. All other engines were varied with respect to the fixed orientation of this engine.

The primary objective of this particular test was to localize the phase angle set that produced a significant reduction in the external sound field; these data sets were to be analyzed in real time such that a crude estimate could be made as to where the global minimal set might reside. A second set of phase angles (tier two data) was then to be performed to attempt to determine the minimal set. However, analysis of the external data in the field proved to be inconclusive and the tests were terminated after the tier one data was acquired for two airspeeds, 115 and 240 knots. These airspeeds represent two typical operational flight conditions. The analysis of the internal data is of primary interest in this thesis. Further analysis of the external data is the subject of ongoing research at the Air Force Research Laboratory.

The system utilized to collect the acoustic information consisted of sixteen Acousti-Cell microphones, a power supply, and a 32-channel METRUM digital tape recorder. The microphones were secured to a cargo strap connected between the paratroop anchor cables that extend the length of the fuselage cabin and positioned slightly above head

height as to not interfere with normal crew operations. In addition to the raw pressure field data from the 16 microphones, channels 17-20 recorded the once-per-revolution signal from each engine to verify that phase control was maintained during measurement. Channel 21 was reserved for an IRIG-B time code signal to synchronize the data upon post-analysis. Unfortunately, the 32-channel METRUM recorder failed during system tuning and a TEAC RX-816 16 channel digital tape recorder had to be installed in its place. With only 16 channels available, five microphone channels had to be sacrificed.

The 11 channels sampled are identified in Figure 2.3.

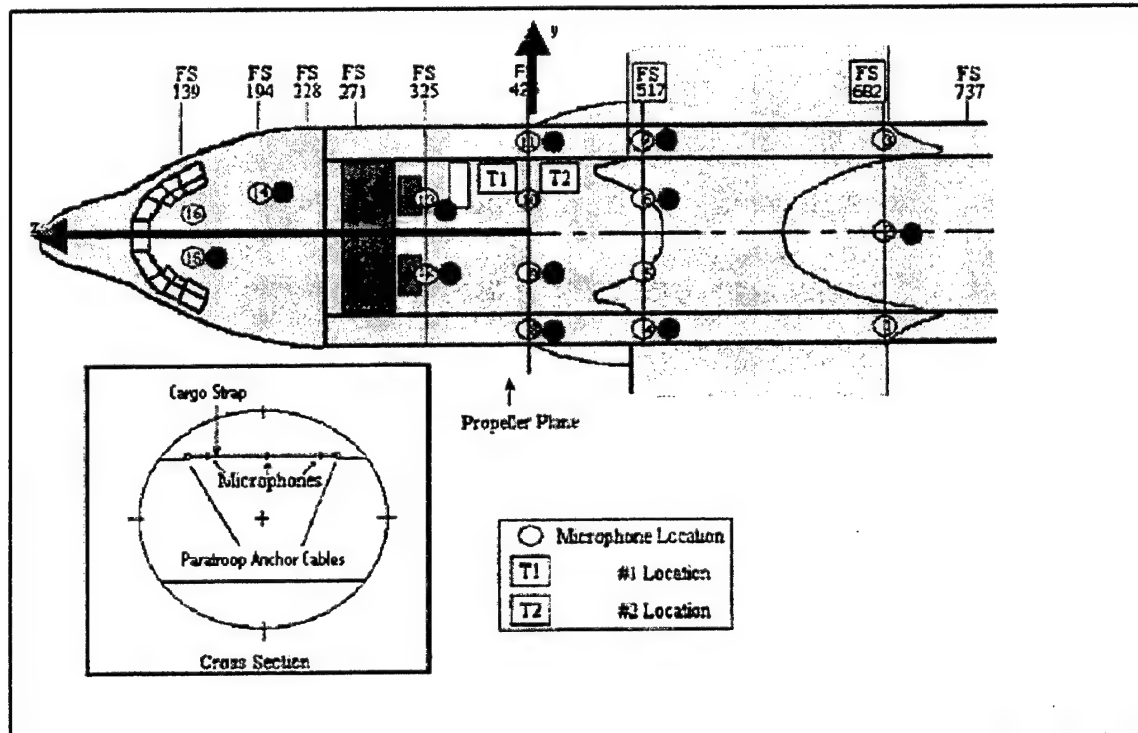


Figure 2.3 Sampled Microphone Fuselage Locations. FS stands for fuselage station and refers to the distance measured from the nose of the aircraft in inches.

These microphone locations were selected in order to prevent the creation of significant holes in the data set. The positions of the cargo bay microphones in a y-z coordinate system centered on the axis of symmetry (z-axis) and the line joining the propeller

centers (y –axis) are represented in Table 2.2. Information from cockpit microphones 14 and 16 will be ignored since the primary concern is cargo bay noise levels. It was assumed that microphones 8-11 resided in the propeller plane of rotation since the separation was much less than one wavelength. Signals were recorded once per revolution on channels 1, 3, 6, 10 and the IRIG-B signal was recorded on channel 16. The PC controller, power supply and other recording equipment were positioned at T1 and T2.

Mic Number	y coord(m)	z coord (m)
8	-1.07	0.00
9	-0.53	0.00
11	1.04	0.00
2	0.00	-6.53
4	-1.07	-2.34
6	0.53	-2.34
7	1.07	-2.34
12	-0.53	2.54
13	0.53	2.54

Table 2.2 Y-Z Coordinates of Cargo Bay Microphone Locations.

Each microphone was calibrated using a 114 dB, 250 Hz tone before each test flight and the respective Engineering Unit (EU) scale factors for each microphone were recorded to facilitate post-analysis. All microphone operations were validated against a gold standard microphone calibrated by the National Institute of Standards. Laboratory analysis of the recorded data was conducted using two HP35665A Dynamic Signal Analyzers (DSAs). The DSAs were configured to process the raw data over a frequency range of 10 Hz to 16 kHz referencing the EU scale factor recorded in the field for each microphone. Both analyzers were set to a 0.25 integration time. A typical one-third-octave band spectrum for the C-130 in standard analog controller configuration (phase angles unknown) is

shown in Figure 2.4 for Microphone seven and a similar plot at the same location is shown in Figure 2.5 for the digital control. (Phase Angles 150°, 180°, 150°, 180°).

In Figure 2.4, the contributions of the BPF at 108 dB are extremely evident as the 63 Hz band is approximately 7 dB above the background jet turbine noise. Information from the 68 Hz BPF appears in the 63 Hz band under one/third octave band analysis. Whereas in Figure 2.5 with the digital synchrophasor engaged, the BPF blends in with the background radiation at a particular phase setting of 150°, 180°, 150°, 180°. There are no observable higher harmonics; if present they are buried within the background radiation. The variance in the data as a function of time for the enhanced controller was generally less than 3 dB. Higher variances occurred on Microphones 4 and 6 near the conclusion of the flight test. These variances were attributed to systematic microphone failure. The data from each microphone for a given phase condition was plotted as a function of position and linearly interpolated using MathCAD to produce contour plots of the acoustic sound field within the fuselage.

Three particular phase angle sets were of interest. The first set (180°, 180°, 180°, 180°) was the condition that should produce constructive interference. The sound field for this set is plotted in Figure 2.6. The second is a combination that reflects destructive interference. Inspection of the plots indicated that a higher degree of destructive interference occurred when the inboard engines are only 30 degrees out of phase. The phase set chosen for comparison (150°, 180°, 150°, and 120°) is plotted in Figure 2.7. The last set chosen for comparison was the phase set that seemed to subjectively

produced the calmest distribution within the fuselage: (180°, 180°, 150°, 120°). See Figure 2.8. The baseline analog controller is illustrated in Figure 2.9. Actual aircraft flyover photos of the aircraft at each phase setting provided verification of phase lock and are compliments of MSgt Alan Martin, AFRL/HECB. All plotted intensities are at the 63 Hz 1/3 octave band (dB) and are plotted against a 1/90 scale aircraft schematic.¹ Cockpit microphone data was not included in the plots.

MC-130E Synchrophaser Flight Test
Microphone 7 - Baseline #2

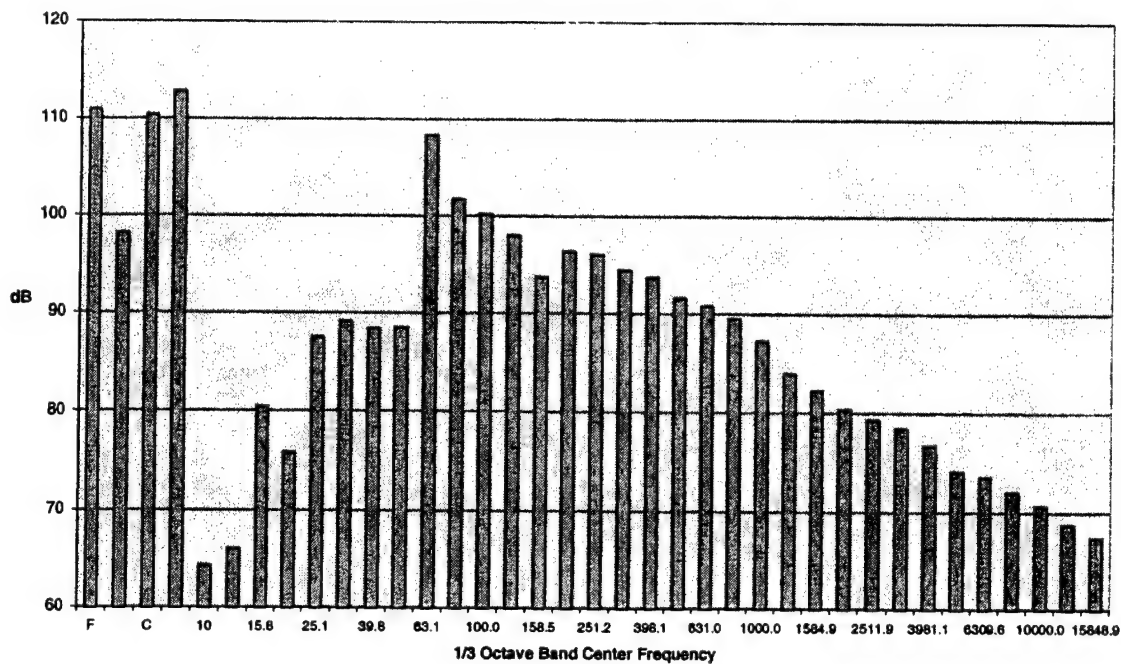


Figure 2.4 One/Third Octave Band Spectra at Microphone Seven - Analog Synchrophaser

MC-130E Synchrophaser Flight Test
Microphone 7 - phase angle 150,180,150,180

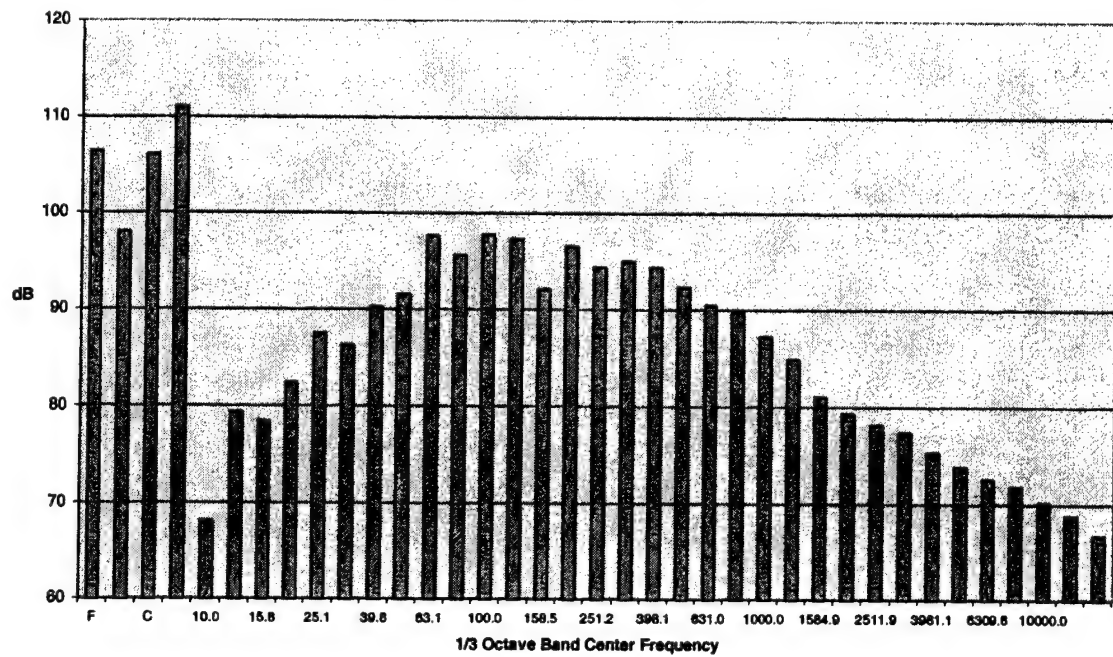


Figure 2.5 One/Third Octave Band Spectra at Microphone Seven - Digital Synchrophaser

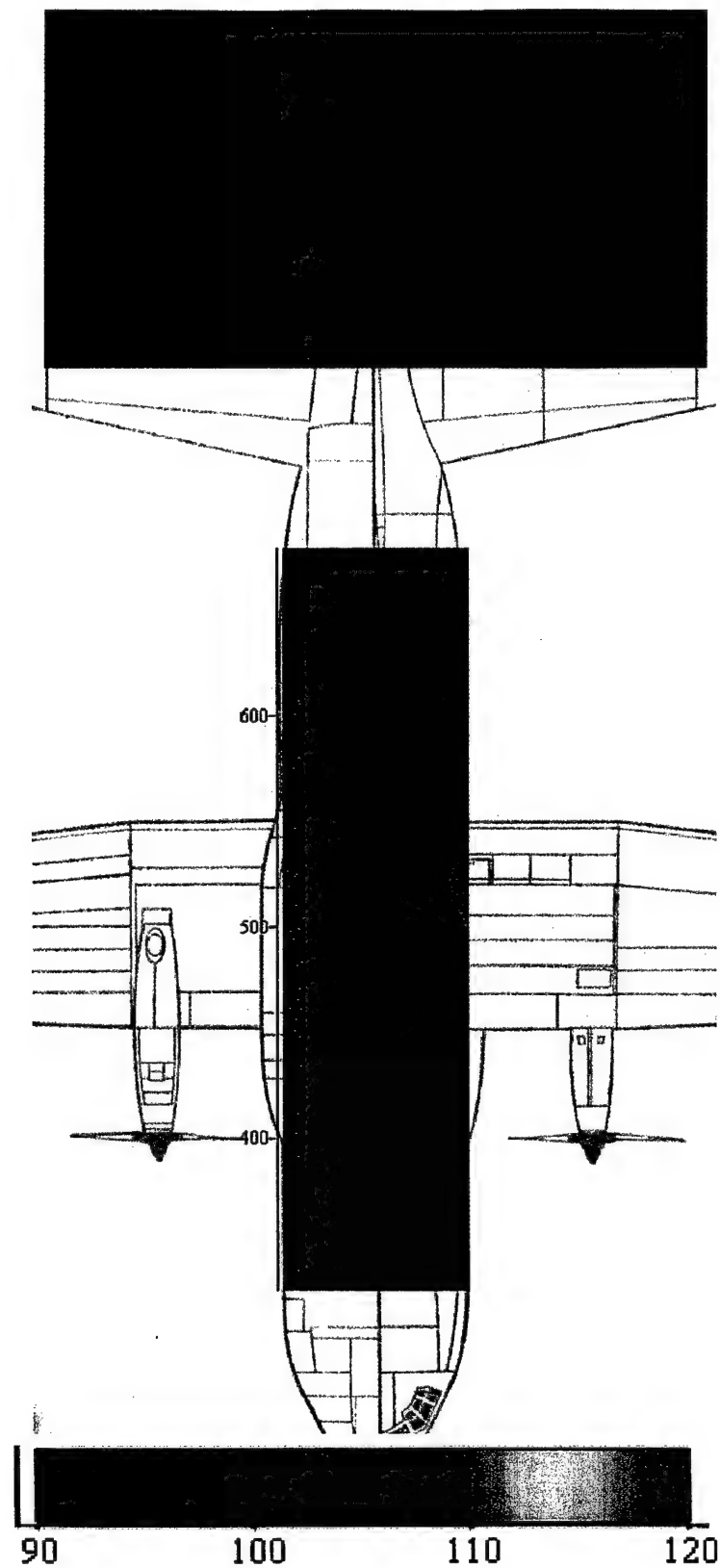


Figure 2.6 Linear Interpolation of the Measured Data - Phase Setting (180°, 180°, 180°, 180°) at 63Hz, One/Third Octave Band (dB)¹ – 240 Knots

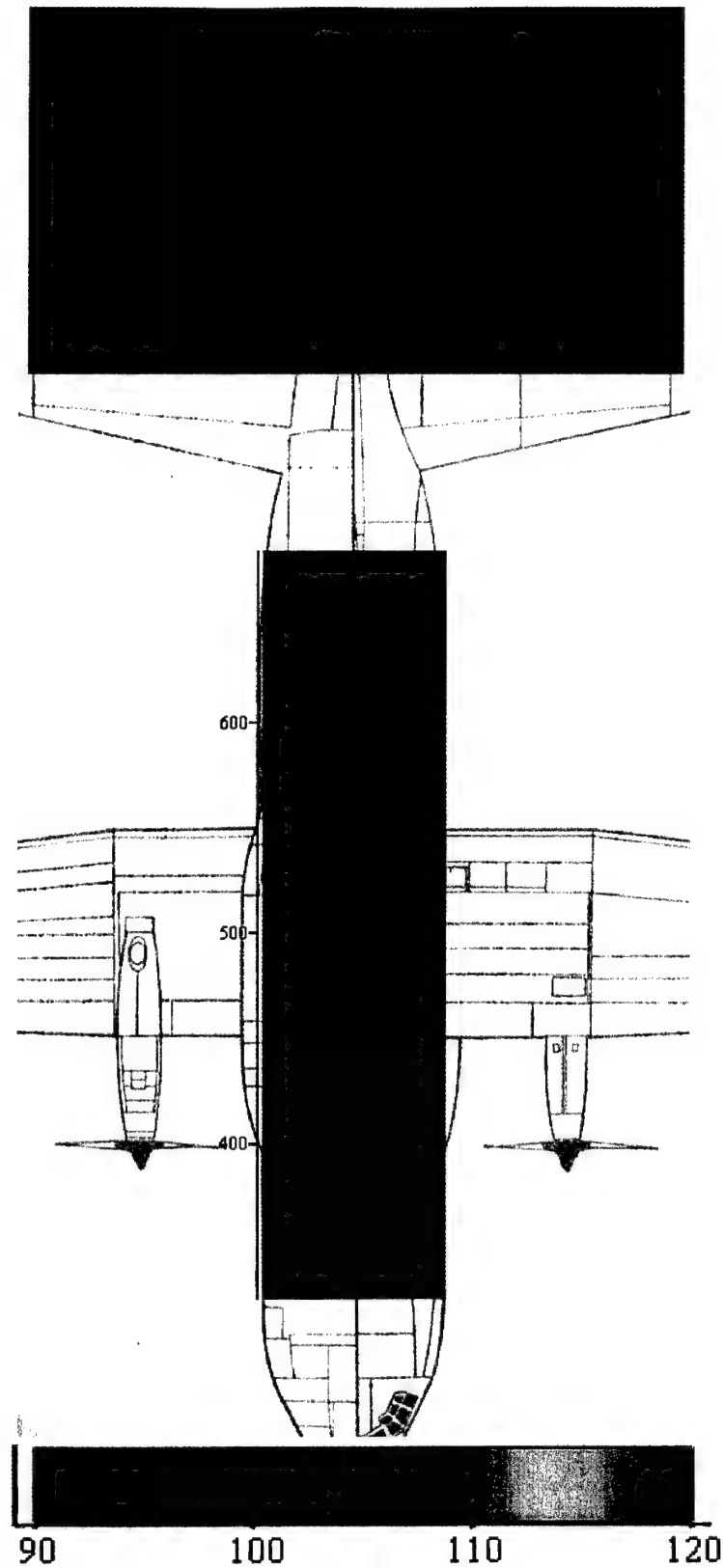


Figure 2.7 Linear Interpolation of the Measured Data - Phase Setting (150°, 180°, 150°, 120°) at 63Hz, One/Third Octave Band (dB) – 240 Knots

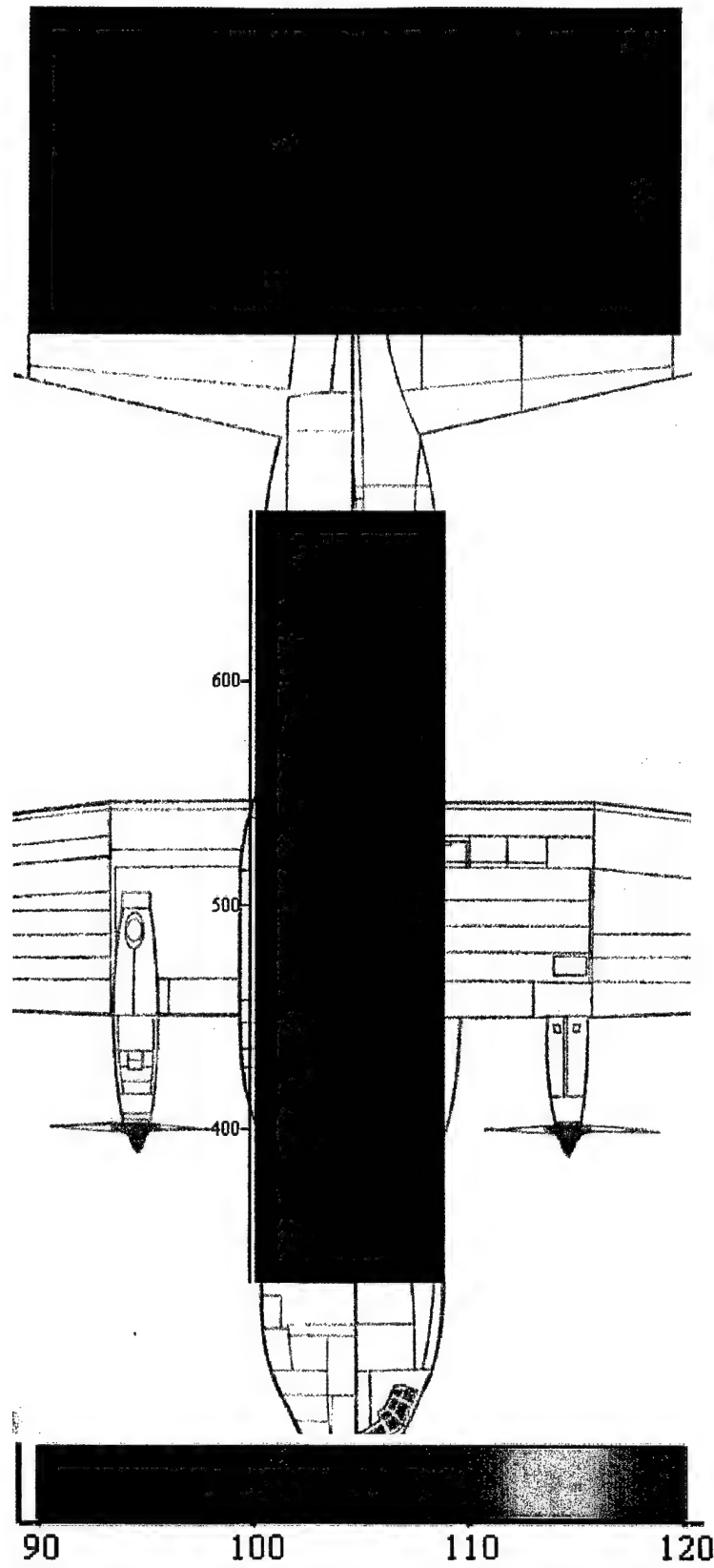


Figure 2.8 Linear Interpolation of the Measured Data - Phase Setting (180°, 180°, 150°, 120°) at 63Hz, One/Third Octave Band (dB) – 240 Knots

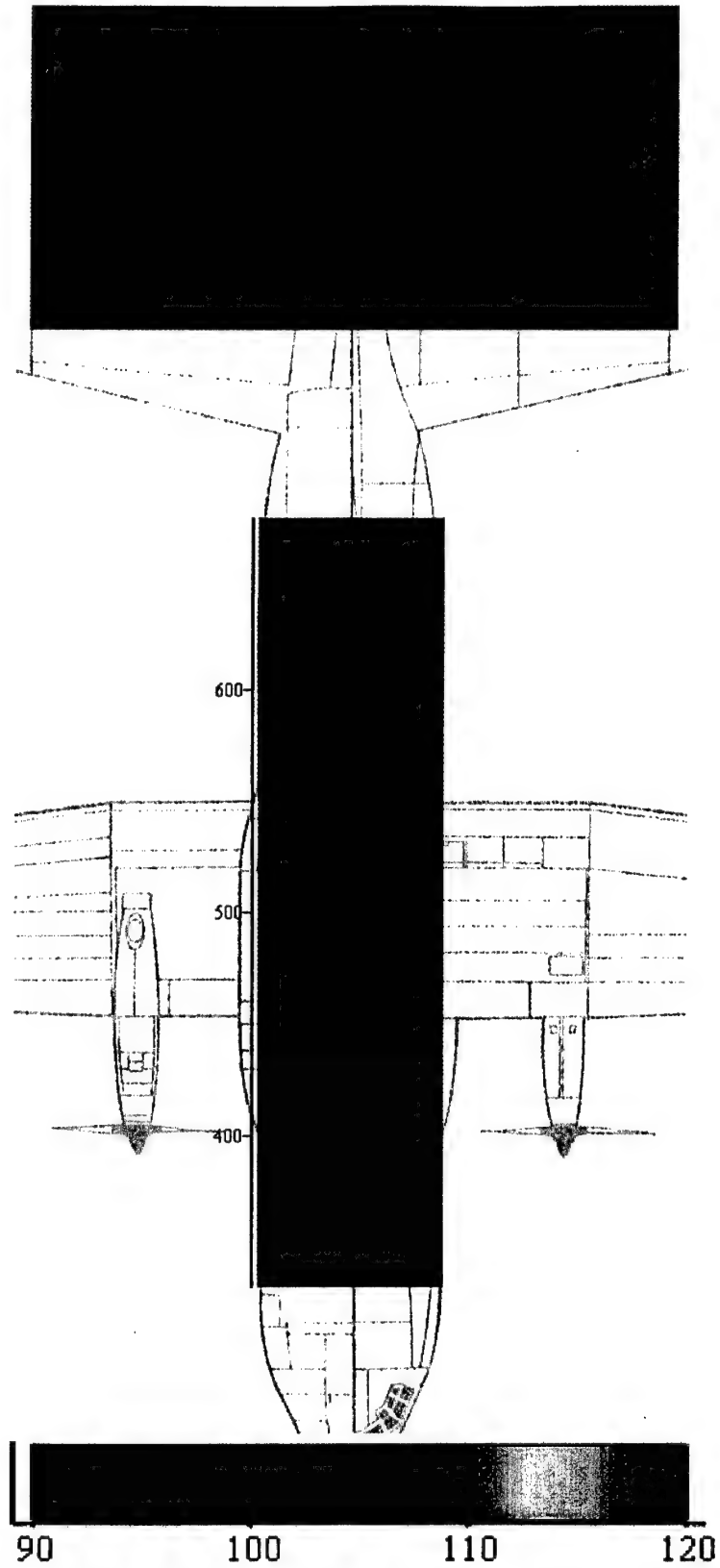


Figure 2.9 Linear Interpolation of the Measured Data -Baseline Analog Controller Configuration at 63Hz, One/Third Octave Band (dB) – 240 Knots

Section 3 - THE ANALYTICAL MODEL

BACKGROUND

In order to develop an analytical model for the acoustic pressure fluctuation, ΔP , at a given point, Q, inside the fuselage, we must first develop a mathematical expression. The most obvious starting point is with the complete lossless inhomogeneous acoustic wave equation,¹²

$$\nabla^2 P - \frac{1}{c^2} \frac{\partial^2 P}{\partial t^2} = -\frac{\partial G}{\partial t} + \nabla \cdot \vec{F} - \frac{\partial^2 (p u_i u_j)}{\partial x_i \partial x_j}, \quad (3.1)$$

where c is the wave speed, G is the rate at which mass is injected into a volume, F is the body force per unit volume, and $\frac{\partial^2 (p u_i u_j)}{\partial x_i \partial x_j}$ is the contribution from viscous forces.

This first term in equation (3.1) above can be eliminated as our propeller source is a rigid body and is not ejecting matter into the fluid. Additionally, the last term can also be eliminated since our source is not the product of spatial rates of change within the fluid as in the exhaust of a jet engine. Thus the only term that survives is the middle term, which represents body forces as those forces produced by moving through a fluid without a change in volume. So we have an inhomogeneous equation of the following form

$$\nabla^2 P - \frac{1}{c^2} \frac{\partial^2 P}{\partial t^2} = \nabla \cdot \vec{F}. \quad (3.2)$$

This equation has the basic structure,

$$\nabla^2 \Psi(\vec{r}, t) - \frac{1}{c^2} \frac{\partial^2 \Psi(\vec{r}, t)}{\partial t^2} = -4\pi f(\vec{r}, t), \quad (3.3)$$

where $f(\vec{r}, t)$ is some source function that includes a spatial and time dependence. It is often customary to solve an equation of this form by developing a Green's function that expresses how the source disturbance will propagate.¹³

To develop the propagator for this case, we first assume that we have a simple system devoid of boundary surfaces. Under these conditions, the explicit time dependence can be eliminated by using the Fourier integral transforms,

$$\begin{aligned}\Psi(\vec{r}, t) &= \frac{1}{2\pi} \int_{-\infty}^{\infty} \Psi(\vec{r}, \omega) \exp(-i\omega t) d\omega \\ f(\vec{r}, t) &= \frac{1}{2\pi} \int_{-\infty}^{\infty} f(\vec{r}, \omega) \exp(-i\omega t) d\omega.\end{aligned}\quad (3.4)$$

By direct substitution of these integrals into our basic equation for the acoustic field (3.3) we arrive at the equation,

$$\nabla^2 \Psi(\vec{r}, \omega) + \frac{\omega^2}{c^2} \Psi(\vec{r}, \omega) = -4\pi f(\vec{r}, \omega), \quad (3.5)$$

Equation 3.5 is merely the nonhomogeneous scalar Helmholtz equation, where $\omega/c = k$, the wave vector associated with the frequency ω .

The Green's function associated with equation (3.5) is

$$(\nabla^2 + k^2) G_k(\vec{r}, \vec{r}') = -4\pi \delta(\vec{r} - \vec{r}'). \quad (3.6)$$

If boundary surfaces are not present, the surface integral in the Green's function vanishes and $G_k(\vec{r}, \vec{r}')$ depends only on the distance between the field point and the source $|\vec{r} - \vec{r}'|$.

The Laplacian operator requires that G_k must satisfy,

$$\frac{1}{(R)} \frac{d^2}{dR^2} (RG_k) + k^2 G_k = -4\pi\delta(\bar{R}), \quad (3.7)$$

where \bar{R} represents the distance from the source point to the observation location, Q.

Hence, we have a general solution that is defined for all points in space except where $R = 0$.

$$RG_k(R) = A \exp(iR) + B \exp(-iR) \quad (3.8)$$

In the limit $R \rightarrow 0$, $kR \ll 1$ and the equation reduces to Poisson's equation. Thus the general normalized solution to the time-independent Green's function is

$$G_k(R) = \frac{A \exp(iR) + B \exp(-iR)}{R}, \quad (3.9)$$

with $A + B = 1$. Now that the time-independent equation has been developed, we need to derive the time-dependent version. (The time independent case will be explored in Model A.)

The corresponding Green's function for the time dependent case must satisfy

$$\left(\nabla_r^2 - \frac{1}{c^2} \frac{d^2}{dt^2} \right) G_k(\bar{r}, t; \bar{r}', t') = \alpha \delta(\bar{r} - \bar{r}') \delta(t - t') \quad (3.10)$$

The time Fourier transform of $G_k(\bar{r}, t; \bar{r}', t')$ can be shown to be $G_k(R) \exp(i\omega t')$. Therefore,

$$\begin{aligned} G_k(\bar{r}, t; \bar{r}', t') &= \frac{1}{2\pi} \int_{-\infty}^{\infty} G_k(R) \exp(i\omega t') \exp(-i\omega t) d\omega, \\ G_k(\bar{r}, t; \bar{r}', t') &= A \frac{\exp(iR)}{R} \delta\left(\tau - \frac{R}{c}\right) + B \frac{\exp(-iR)}{R} \delta\left(\tau + \frac{R}{c}\right), \\ G_k(\bar{r}, t; \bar{r}', t') &= G_k^+(\tau - \frac{R}{c}) + G_k^-(\tau + \frac{R}{c}), \\ G_k(\bar{r}, t; \bar{r}', t') &= G_k^+(R, \tau) + G_k^-(R, \tau), \end{aligned} \quad (3.11)$$

where $\tau = t - t'$.

Expressing the propagator in an explicit form,

$$G_k^{\pm}(R, \tau) = \frac{\delta\left(t' - \left(t \mp \frac{|\vec{r} - \vec{r}'|}{c}\right)\right)}{|\vec{r} - \vec{r}'|} \quad (3.12)$$

We neglect the advanced Green's function $G_k^-(R, \tau)$ because we are only concerned with the particular delta function argument that describes the acoustic field at some observation point Q at time t caused by a disturbance at some distance r away at an earlier time t' . $G_k^+(R, \tau)$ is sometimes called the causal Green's function.¹⁴ Now with the propagator completely defined, we can determine, at least in principle, the acoustic field at any point by integrating the product of our Green's function and the source function, S, over all space and time, neglecting surface effects:

$$\Delta P(\vec{r}, t) = \iint G_k^+(\vec{r}, t; \vec{r}', t') S(\vec{r}', t') d\vec{r}' dt'. \quad (3.13)$$

At this point, the model development becomes a little more complicated as the wavelength ($\lambda = 5m$) is on the same order as $|\vec{r} - \vec{r}'|$. This region of interest is generally referred to as the intermediate or induction zone¹⁵ and makes evaluation of the integral in (3.13) difficult. The neglect of any surface present means that refraction and reflection effects will be ignored. These effects are considered small since the relevant wavelength is an order of magnitude larger than the thickness of the fuselage skin.

In the remainder of this section, three models will be developed based upon the foregoing discussion.

MODEL A – Monochromatic Point Source

In our first attempt at modeling the system, we shall take a simple case that should be relatively easy to evaluate, namely, treating the engines as point sources having a harmonic time dependence $\exp(i(\omega t - \phi_i))$ where ω is the BPF (68Hz) and ϕ_i is the phase angle of the i^{th} engine ($i = 1-4$). In this case, the source term for the i^{th} engine can be written,

$$S_i(\vec{r}, t) = S_i \delta(\vec{r} - \vec{r}_i') \exp(-i(\omega t - \phi_i)) \quad (3.14)$$

where the constant S_i denotes the acoustic strength for propeller noise associated with engine i centered at \vec{r}' . From equation (3.13) we obtain the effect of a point source at engine i on the acoustic amplitude at a point \vec{r} and at a time t ,

$$\Delta P_i(\vec{r}, t) = \frac{S_i \exp(i\phi_i) \exp(ik|\vec{r} - \vec{r}_i'|)}{|\vec{r} - \vec{r}_i'|} \exp(-i\omega t), \quad (3.15)$$

$$\text{where } k = \frac{\omega}{c}.$$

The combined effect of the four engines is, by superposition,

$$\Delta P_i(\vec{r}, t) = \exp(-i\omega t) \sum_{i=1}^4 \frac{S_i \exp(i\phi_i) \exp(ik|\vec{r} - \vec{r}_i|)}{|\vec{r} - \vec{r}_i|}. \quad (3.16)$$

The sound intensity $I(\vec{r})$ at the observation point \vec{r} , averaged over one cycle, is proportional to,

$$|\overline{\Delta P_i(\vec{r}, t)}|^2 = \sum_{i,j=1}^4 \frac{S_i S_j * \exp(i(k|\vec{r} - \vec{r}_i| + \phi_i) - i(k|\vec{r} - \vec{r}_j| + \phi_j))}{|\vec{r} - \vec{r}_i| |\vec{r} - \vec{r}_j|} \quad (3.17)$$

$$|\overline{\Delta P_i(\vec{r}, t)}|^2 = |S|^2 \left\{ \sum_{i=1}^4 \frac{1}{|\vec{r} - \vec{r}_i|^2} + 2 \sum_{i>j}^4 \frac{\cos[(k|\vec{r} - \vec{r}_i|) - (k|\vec{r} - \vec{r}_j|) + (\phi_i - \phi_j)]}{|\vec{r} - \vec{r}_i| |\vec{r} - \vec{r}_j|} \right\}, \quad (3.18)$$

assuming the sources are all of equal strength, S .

Equation (3.18) was used to calculate the relative acoustic intensity at an array of points within the fuselage of the aircraft. Since the experimental data is recorded in decibels (dB), the calculated values were scaled according to,

$$I(\text{dB}) = \text{scale_factor} + \left(10 \log \left(\frac{I}{I_{\text{ref}}} \right) \right), \quad (3.19)$$

where I_{ref} was taken to be 20 micropascals and the scale factor was chosen to make the $I(\text{dB})$ fall within the range of the experimental data set (90 to 120 dB). With the values calculated for the acoustic intensity the data was interpolated in the same manner as the actual data sets. Representative cases are included in Figures 3.1-3.4.

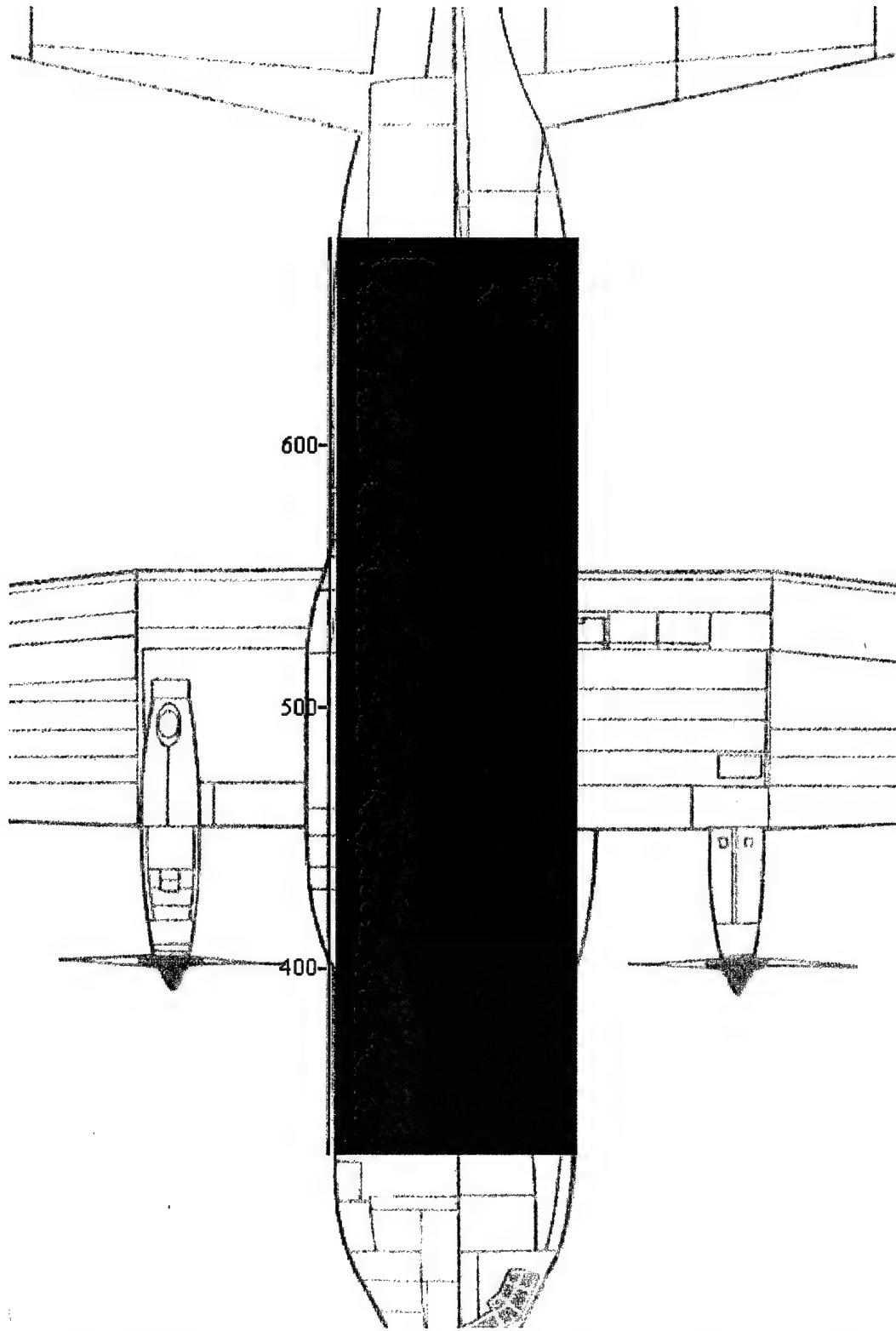


Figure 3.1. Predicted Fuselage Acoustic Intensity - Model A (Point Source) - Phase Angle (180°, 180°, 180°, 180°).

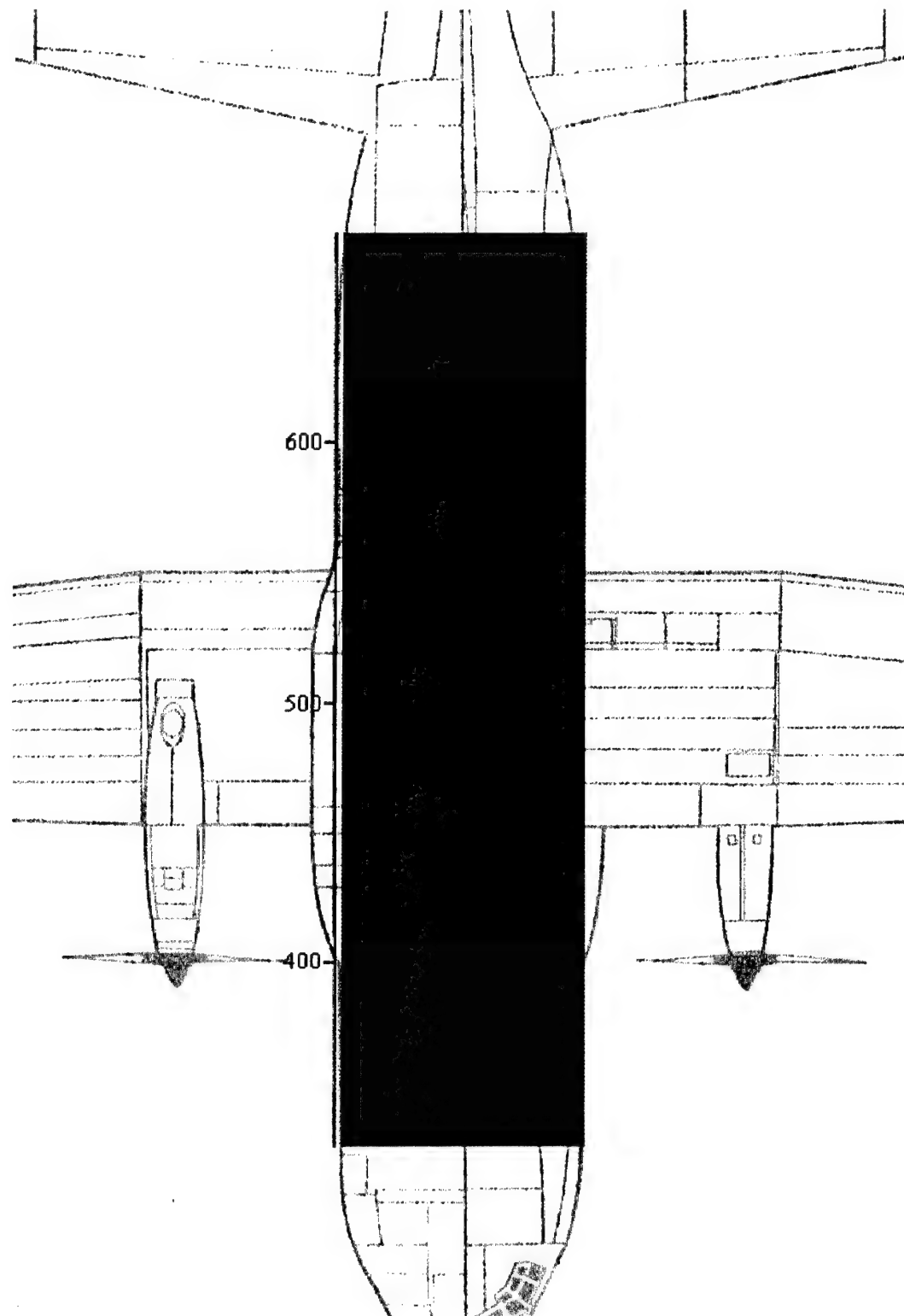


Figure 3.2. Predicted Fuselage Acoustic Intensity - Model A (Point Source) - Phase Angle (150°, 180°, 150°, 120°)

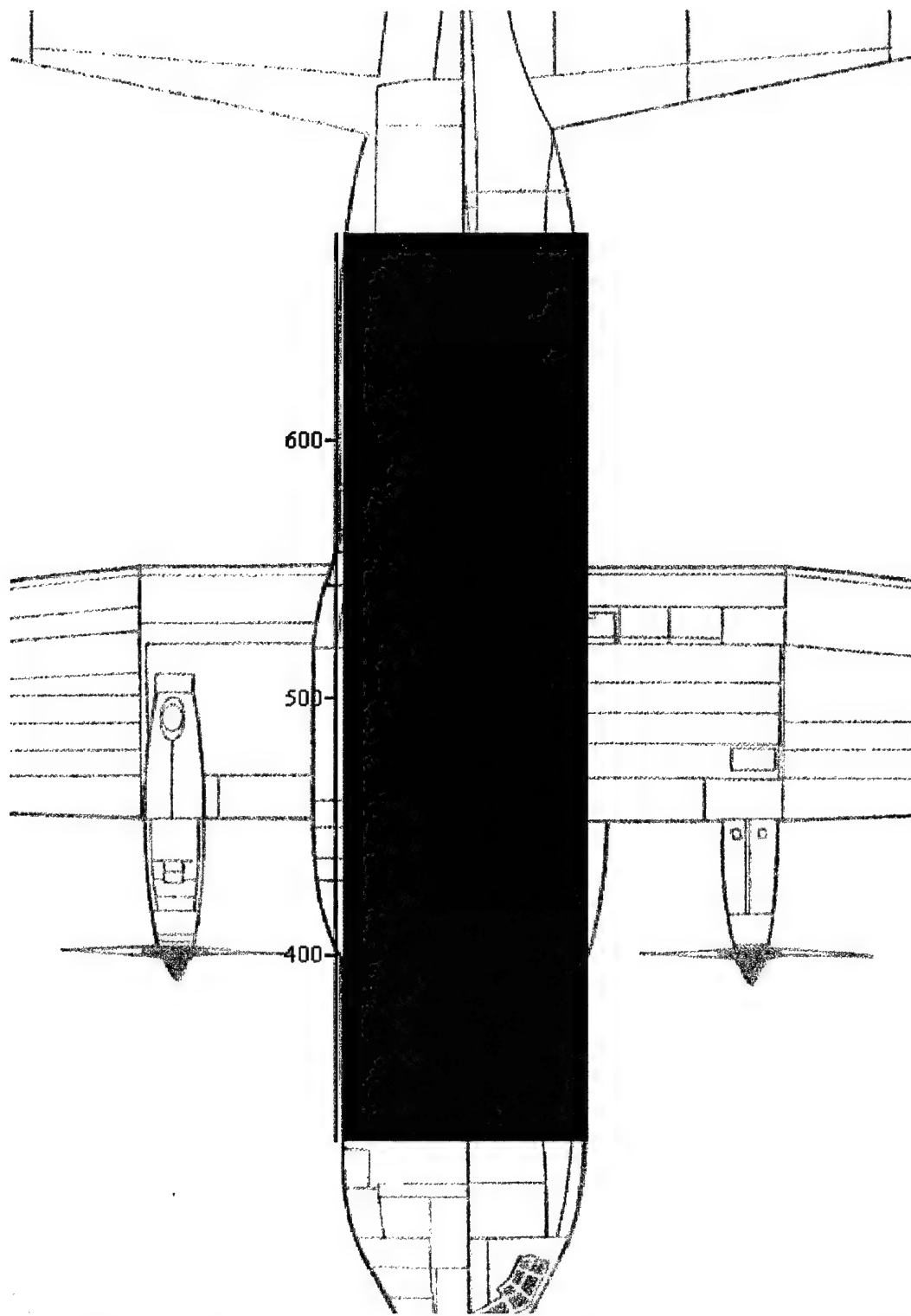


Figure 3.3.10 Predicted Fuselage Acoustic Intensity - Model A (Point Source) - Phase Angle (180°, 180°, 150°, 120°)

MODEL B – Extended Source Function

Consider now that each propeller assembly can be visualized as a pulsating disk of radius “ a ”, constrained to the plane of rotation of the propeller assembly. See Figure 3.4.

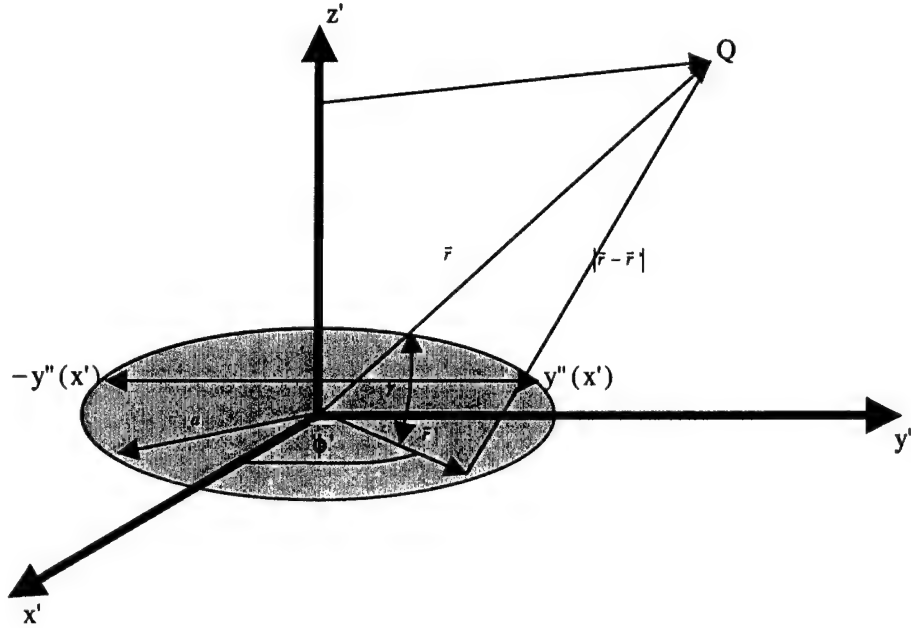


Figure 3.4. Pulsating Disk Propeller Assembly Representation

In addition to being an extended rather than a point source, the time dependence, $f(t')$, although assumed periodic with a period equal to the BPF, will not be restricted to being harmonic. Thus,

$$S(\vec{r}, t) = S(x', y') \delta(z') f(t'), \quad (3.20)$$

where the primed indices denote the source coordinates and the Dirac delta function in 3.25 guarantees no z' contribution. If $f(t')$ is non-harmonic there will be, in addition to the fundamental, $\omega_1 = BPF$, higher harmonics contributing to the acoustic signal.

We assume that $S(x', y')$ is radially symmetric in the $x'y'$ plane about the propeller hub.

Then inserting the source function into 3.18 and integrating over z' and t' yields,

$$\Delta P(\vec{r}, t) = \int_0^{2\pi} \int_0^a \frac{S(r')}{|\vec{r} - \vec{r}'|} f\left(t - \frac{|\vec{r} - \vec{r}'|}{c}\right) r' dr' d\phi'. \quad (3.21)$$

Expressing the time contribution as a Fourier series,

$$f(t) = \sum_{-\infty}^{\infty} C_n \exp(-i\omega_n t) \exp(i\phi), \quad (3.22)$$

where C_n is the n^{th} Fourier component, $\omega_n = n\omega$ and ϕ is a phase angle, $\Delta P(\vec{r}, t)$ can be written as,

$$\Delta P(\vec{r}, t) = \exp(i\phi) \sum_{-\infty}^{\infty} C_n \exp(-i\omega_n t) S_n(\vec{r}), \quad (3.23)$$

where

$$S_n(\vec{r}) = \int_0^{2\pi} \int_0^a \frac{S(r')}{|\vec{r} - \vec{r}'|} \exp(ik_n |\vec{r} - \vec{r}'|) r' dr' d\phi, \quad (3.24)$$

and $k_n = \frac{n\omega}{c}$.

If we denote by the index "j" the contribution from the j^{th} engine, then the total pressure fluctuation at the observation point \vec{r} at a time t is

$$\Delta P(\vec{r}, t) = \sum_{j=1}^4 \Delta P_j(\vec{r}, t) \quad (3.25)$$

Multiplying this expression by its complex conjugate and taking the time average over a period T gives

$$\overline{|\Delta P(\vec{r}, t)|^2} = \frac{1}{T} \sum_{j=1}^4 \sum_{j'=1}^4 \exp(i\varphi_j) \exp(-i\varphi_{j'}) \sum_{n=1}^{\infty} S_n(\vec{r}) \sum_{n'=1}^{\infty} S_{n'}^*(\vec{r}) C_n C_{n'}^* \int_0^T \exp(-it(\omega_n - \omega_{n'})) dt$$

By virtue of orthogonality , only the terms with $n=n'$ survive. Hence,

$$\left| \overline{\Delta P(r,t)} \right|^2 = \sum_{n=0}^{\infty} |C_n|^2 \left| \sum_{j=1}^4 \exp(i\varphi_j) S_{nj}(\vec{r}) \right|^2 \quad (3.26)$$

Now all that remains is to evaluate the $S_{nj}(\vec{r})$. We shall assume that $S(r')$ is a constant, S_0

Referring to Figure 3.4, the distance between a field point \vec{r} and a source point \vec{r}' can be expressed as a series of Legendre polynomials,

$$\frac{1}{|\vec{r}-\vec{r}'|} = \frac{1}{r} \sum_{L=0}^{\infty} P_L(\gamma) \left(\frac{r'}{r} \right)^L, \quad (3.27)$$

where γ is the angle between \vec{r} and \vec{r}' . The series converges as long r is greater than r' .

In the integral expression (3.24) for $S_{nj}(\vec{r})$, r' is restricted to $0 < r' < a$, whereas r is always greater than a . In the integral we will consider only the first two terms in the expansion,

$$\frac{1}{|\vec{r}-\vec{r}'|} \approx \frac{1}{r} \left((P_0(\gamma) + P_1(\gamma) \frac{r'}{r}) \right) = \frac{(r + r' \cos(\gamma))}{r^2}. \quad (3.28)$$

Likewise the exponential term in (3.24) can be written,

$$|\vec{r}-\vec{r}'| \approx \frac{r}{1 + \frac{r'}{r} \cos(\gamma)} \approx r \left(1 - \frac{r'}{r} \cos(\gamma) \right) = r - r' \cos(\gamma). \quad (3.29)$$

Expressing \vec{r} and \vec{r}' in cartesian component form, an expression for cosine (γ) can be developed in terms of y , r , y' , and r' .

$$\vec{r}' \cdot \vec{r} = r' r \cos \gamma = ((r \sin \theta) \hat{j}' + (r \cos \theta) \hat{k}') \cdot ((r \sin \phi') \hat{j} + (r' \sin \phi) \hat{i}) = (y \hat{j}' + z \hat{k}') \cdot (y \hat{j} + x \hat{i})$$

$$\cos(\gamma) = \frac{y' \cdot y}{r' \cdot r} \quad (3.30)$$

Substituting back into the equation 3.24 for S_n ,

$$S_n = \frac{S_0}{r^2} \cdot \int_0^a \int_0^{2\pi} (r + r' \cdot \cos(\gamma)) \exp[i \cdot k_n(r - r' \cdot \cos(\gamma))] \cdot r' dr' d\phi$$

$$S_n = \frac{S_0}{r^2} \cdot \int_0^a \int_0^{2\pi} \left[r + r' \cdot \left(\frac{y}{r}, \frac{y'}{r'} \right) \right] \exp \left[i \cdot k_n \left[r - r' \cdot \left(\frac{y}{r}, \frac{y'}{r'} \right) \right] \right] \cdot r' dr' d\phi$$

$$S_n = \frac{S_0}{r^3} \cdot \int_{-a}^a \int_{-y''(x')}^{y''(x)} (r^2 + y \cdot y') \exp \left[i \cdot k_n \left[\frac{(r^2 - y \cdot y')}{r} \right] \right] dy' dx'$$

$$S_n = \frac{S_0 \cdot \exp(i \cdot k_n \cdot r)}{r^3} \cdot \int_{-a}^a \int_{-y''(x)}^{y''(x)} (r^2 + y \cdot y') \cdot \exp \left(-i \cdot k_n \frac{y \cdot y'}{r} \right) dy' dx'$$

$$S_n = \frac{S_0 \cdot \exp(i \cdot k_n \cdot r)}{r^3} \cdot \int_{-a}^a \int_{-y''(x)}^{y''(x)} (r^2 \cdot \exp(-i \cdot \alpha y') + y \cdot y' \cdot \exp(-i \cdot \alpha y')) dy' dx'$$

$$S_n = \frac{S_0 \cdot \exp(i \cdot k_n \cdot r)}{r^3} \cdot (r^2 \cdot I_1 + y I_2)$$

where $\alpha = k_n y / r$, $y''(x') = (a^2 - x'^2)^{1/2}$ (Figure 3.4), and “a” is taken to be the propeller radius (2 m). Now all that remains is to evaluate each of the double integrals I_1 and I_2 .

Performing the first integration over y' on integral I_1 ,

$$\begin{aligned}
I_1 &= \int_{-a}^a \int_{-y''(x)}^{y''(x)} \exp(-i\cdot\alpha\cdot y') dy' dx' \\
I_1 &= \int_{-a}^a (\exp(-i\cdot\alpha\cdot y'') - \exp(i\cdot\alpha\cdot y'')) \cdot \frac{1}{-i\cdot\alpha} dx' \\
I_1 &= \int_{-a}^a 2 \cdot \frac{\sin(\alpha \cdot y'')}{\alpha} dx' \\
&\quad (3.31)
\end{aligned}$$

Evaluating the I_2 term in the same manner,

$$\begin{aligned}
I_2 &= \int_{-a}^a \int_{-y''(x')}^{y''(x')} y' \cdot \exp(-i\cdot\alpha\cdot y') dy' dx' \\
I_2 &= \int_{-a}^a \left[\frac{(i\cdot y''(x)\cdot\alpha + 1)}{\alpha^2} \cdot \exp(-i\cdot y''(x)\cdot\alpha) + \exp(i\cdot y''(x)\cdot\alpha) \cdot \frac{(i\cdot y''(x)\cdot\alpha - 1)}{\alpha^2} \right] dx' \\
I_2 &= \frac{2i}{\alpha^2} \cdot \int_{-a}^a (y''(x)\cdot\alpha \cdot \cos(y''(x)\cdot\alpha) - \sin(y''(x)\cdot\alpha)) dx' \\
&\quad (3.32)
\end{aligned}$$

The remaining integral over x' cannot be done analytically for either I_1 or I_2 , so a numerical method was used.

In the same manner as for Model A, MathCAD was utilized to manipulate the arrays and generate values for the acoustic intensity for each observation point. Since the experimental data does not indicate higher order harmonics, only the contributions of the

fundamental frequency (BPF) of 68 Hz was considered. Plots of the model results at the three phase angle sets defined in the Experimental section are shown in Figures 3.5- 3.7.

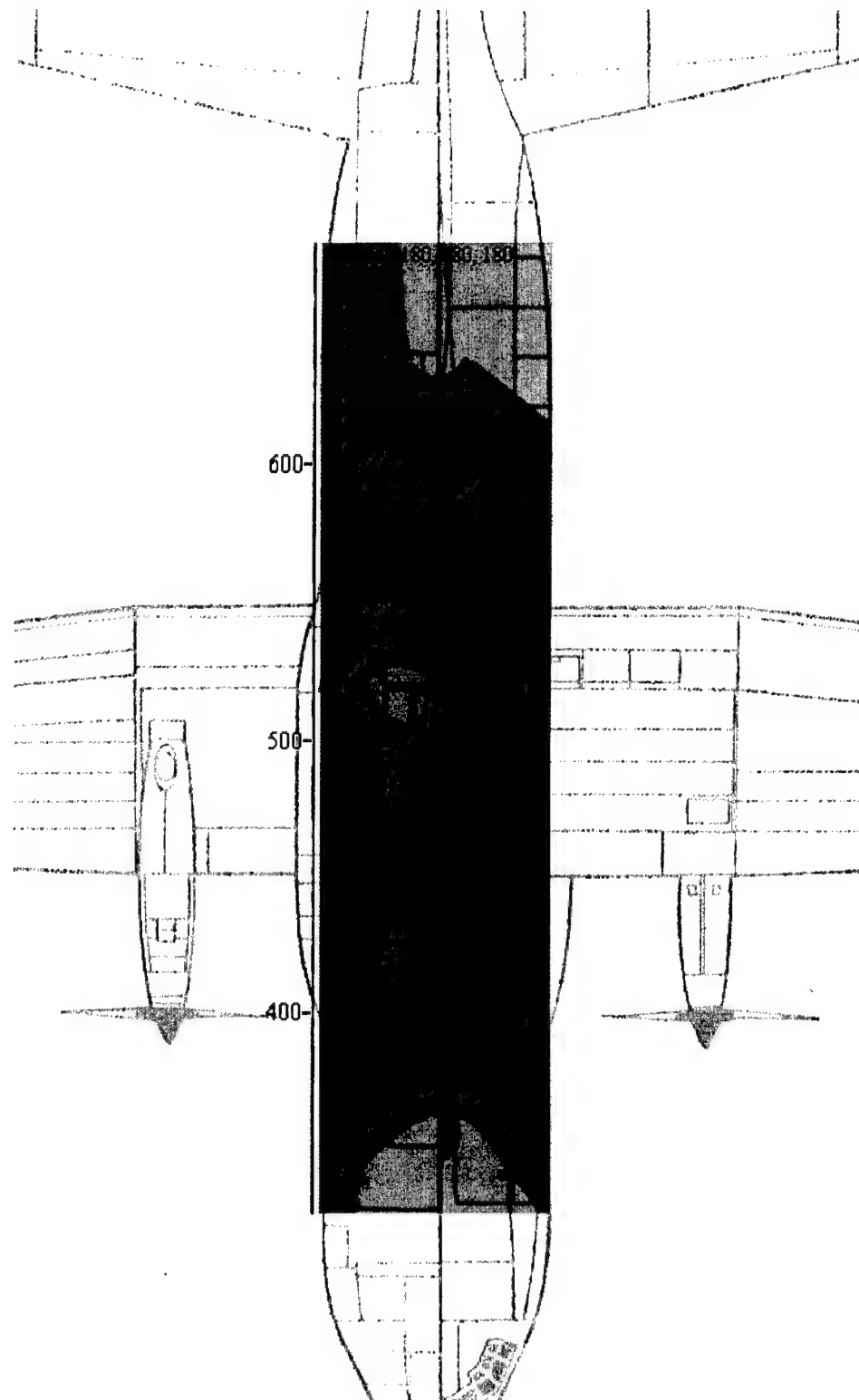


Figure 3.5. Predicted Fuselage Acoustic Intensity - Model B (Radiating Disk) - Phase Angle (180°, 180°, 180°)

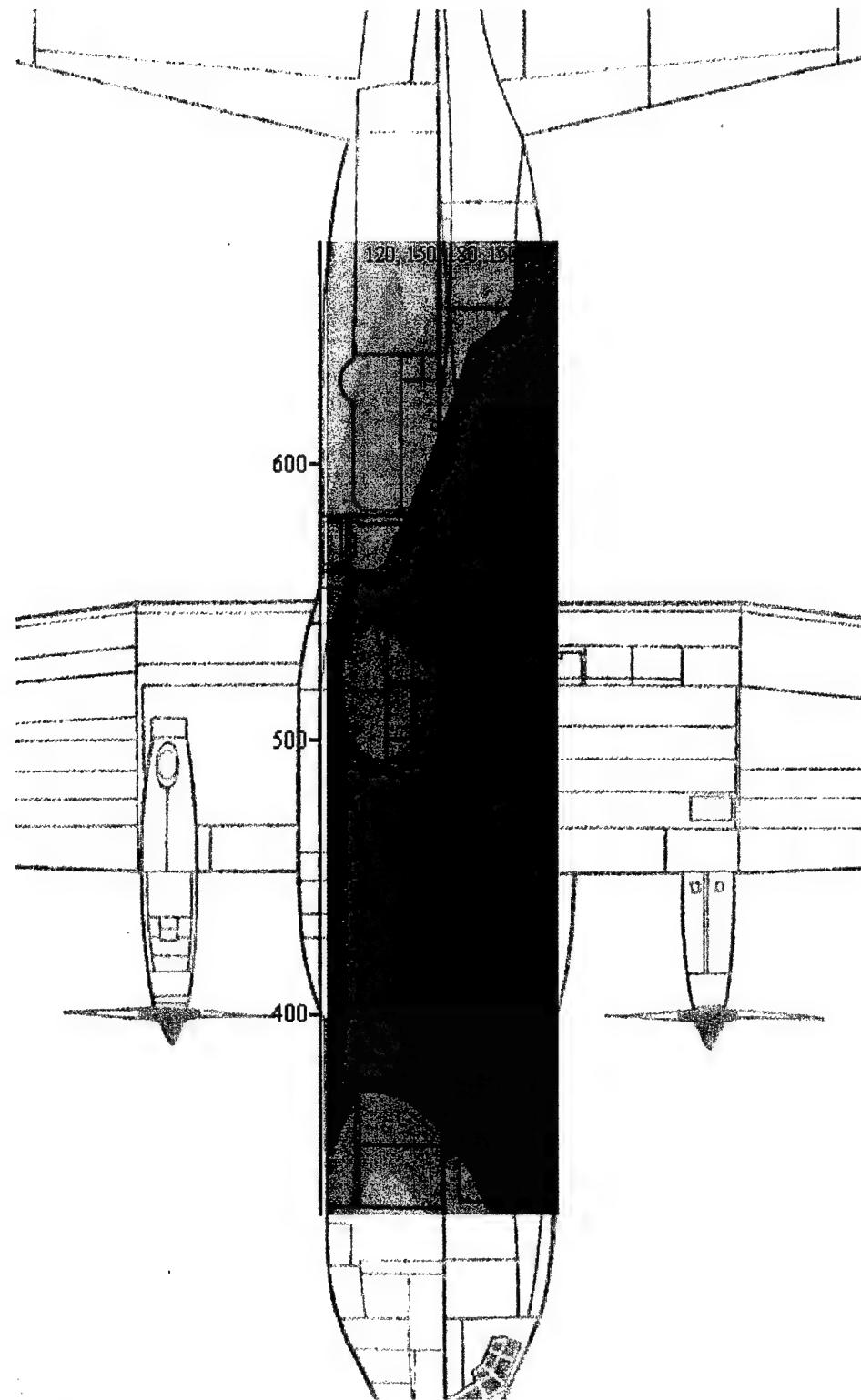


Figure 3.6. Predicted Fuselage Acoustic Intensity - Model B (Radiating Disk) -Phase Angle (150°, 180°, 150°, 120°)

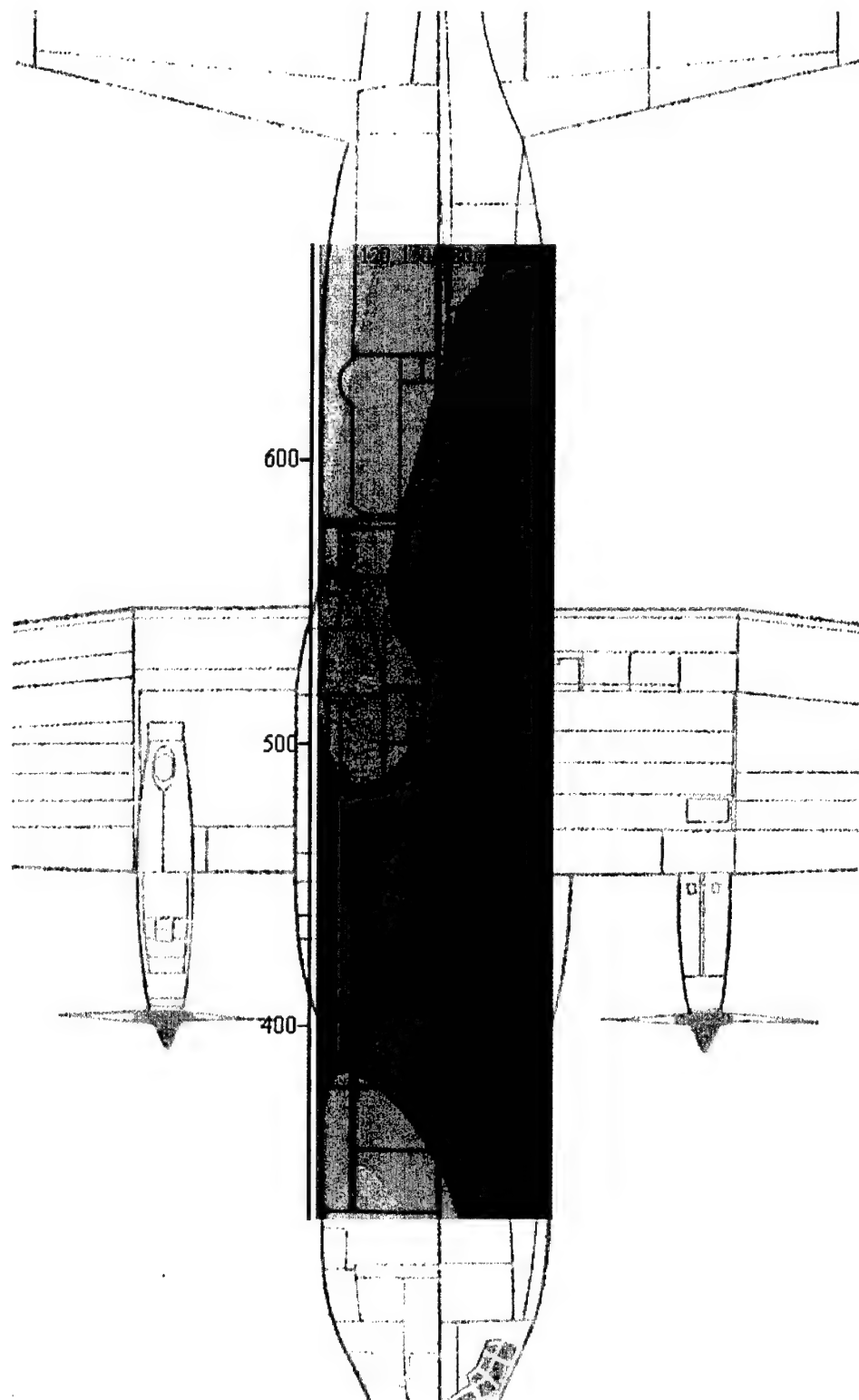


Figure 3.7. Predicted Fuselage Acoustic Intensity - Model B (Radiating Disk) - Phase Angle (180°, 150°, 120°)

Model C – Uniformly Rotating Paddle

Instead of a pulsating disk as in Figure 3.4, envision the source as a single propeller of radius “a” confined to rotate about the hub at a frequency ω equal to the BPF. From the acoustic wave equation (3.1), we identify the source of the radiation as a body force density $\vec{F}(\vec{r},t)$ which actually arises from a paddle-air contact force at the paddle surface. For simplicity, we consider the contact force as acting only along the blade of the paddle (assumed infinitesimally thin), with a magnitude at each point on the blade proportional to the blade velocity, i.e.

$$\vec{F}_{Contact} \text{ per unit length of the blade} = \kappa \vec{v}(\vec{r}) = k(\vec{\omega} \times \vec{r}) = k\omega\rho\hat{\phi}, \quad 0 < \rho < a,$$

where κ is the force coefficient per unit length and the polar coordinates ρ and ϕ ($=\omega t - \delta$) locate the point on the blade. Here δ is the phase angle of the rotating paddle. The total body force is therefore,

$$\vec{F}_{Total} = \int_0^a \kappa \omega \rho \hat{\phi} d\rho \quad (3.33)$$

By definition, \vec{F}_{Total} can be written as a volume integral over the body force density $\vec{F}(\vec{r},t)$, so in cylindrical coordinates (ρ, ϕ, z) we have,

$$\vec{F}_{Total} = \int_0^\infty \int_0^\infty \int_0^{2\pi} \rho \vec{F}(\vec{r},t) \rho d\rho d\phi dz \quad (3.34)$$

Equating the two expressions (3.33) and (3.34) shows that $\vec{F}(\vec{r},t)$ must have the representation,

$$\begin{aligned} \vec{F}(\vec{r},t) &= \kappa \omega \hat{\phi} \delta(z) \delta(\phi - \omega t + \delta) \text{ if } (0 \leq \rho \leq a) \\ \vec{F}(\vec{r},t) &= 0 \text{ if } (\rho > a) \end{aligned} \quad (3.35)$$

The delta function over z restricts the body force density to the x - y plane. The other delta function ensures periodicity and eliminates harmonic contributions. Since \vec{F} has only an azimuthal component, the source term for the inhomogeneous acoustic wave equation (3.2) is

$$\begin{aligned}\nabla \cdot \vec{F}(\vec{r}, t) &= \frac{1}{\rho} \frac{d}{d\phi} (\kappa \omega \delta(z) \delta(\varphi - \omega t + \delta)) \\ \nabla \cdot F(\vec{r}, t) &= \frac{1}{\rho} \kappa \omega \delta(z) \delta'(\varphi - \omega t + \delta)\end{aligned}\quad (3.36)$$

Substituting our source term into equation 3.13,

$$\Delta P(\vec{r}, t) = \kappa \omega \int_{-\infty}^{\infty} \int_0^{\infty} \frac{1}{\rho'} \frac{\delta(z')}{|\vec{r} - \vec{r}'|} \delta'(\varphi' - \omega t + \delta) \delta\left(t' - t + \frac{|\vec{r} - \vec{r}'|}{c}\right) dt' d\vec{r}'$$

Integrating over t' is straightforward,

$$\Delta P(\vec{r}, t) = \kappa \omega \int_0^{\infty} \frac{1}{\rho'} \frac{\delta(z')}{|\vec{r} - \vec{r}'|} \delta'(\varphi' - \omega t_{rel} + \delta) d\vec{r}', \quad (3.37)$$

where,

$$t_{rel} = t - \left(\frac{|\vec{r} - \vec{r}'|}{c} \right).$$

Integration over z' gives

$$\Delta P(\vec{r}, t) = \kappa \omega \int_0^a \int_0^{2\pi} \frac{1}{|\vec{r} - \vec{r}'|} \delta'(\varphi' - \omega t_{rel} + \delta) d\phi' d\rho', \quad (3.38)$$

Before we can proceed further, we express the quantity $|\vec{r} - \vec{r}'|$ in the integrand in cylindrical coordinates,

$$\Delta P(\vec{r}, t) = \kappa \omega \int_0^a \int_0^{2\pi} \frac{1}{\sqrt{r^2 + \rho'^2 - 2\rho' (x \cos(\phi) + y \sin(\phi))}} \delta'(\varphi' - \omega t_{rel} + \delta) d\phi' d\rho',$$

using the component expansions of \mathbf{r} and \mathbf{r}' ,

$$\begin{aligned}\vec{r}' &= \rho' \cos(\phi') \hat{x} + \rho' \sin(\phi') \hat{y} \\ \vec{r} &= x \hat{x} + y \hat{y} + z \hat{z}.\end{aligned}$$

We are ready to integrate over ϕ' .

Integration involving a delta function derivative is simply the negative of the derivative of the function evaluated at the argument of the delta function. Thus,

$$\Delta P(\vec{r}, t) = \kappa \omega \int_0^a \frac{\rho' (x \sin(\omega t_{\text{ret}} - \delta) - y \cos(\omega t_{\text{ret}} - \delta))}{\left(r^2 + \rho'^2 - 2\rho' (x \cos(\omega t_{\text{ret}} - \delta) + y \sin(\omega t_{\text{ret}} - \delta)) \right)^{3/2}} d\rho',$$

If t_{ret} is independent of ρ' , then γ is also independent of ρ' and the quantity in parentheses in the numerator is a constant in the integration. The denominator is merely the distance between the source and the observation point; therefore we may rewrite the integral as,

$$\Delta P(\vec{r}, t) = C \int_0^a \frac{\rho'}{\left(r^2 + \rho'^2 - 2\rho' \cos(\gamma) \right)^{3/2}} d\rho', \quad (3.39)$$

where,

$$\cos(\gamma) = \frac{x \cdot \cos(\omega t_{\text{ret}} - \delta) + y \cdot \sin(\omega t_{\text{ret}} - \delta)}{r}$$

and

$$C = \kappa \cdot \omega (x \cdot \cos(\omega t_{\text{ret}} - \delta) - y \cdot \sin(\omega t_{\text{ret}} - \delta))$$

Making the substitution $u = \rho' - r \cos(\gamma)$ gives

$$\Delta P(\vec{r}, t) = C \int_{-r \cos(\gamma)}^{a - r \cos(\gamma)} \frac{u + r \cos(\gamma)}{\left(u^2 + r^2 \sin^2(\gamma) \right)^{3/2}} du$$

$$\Delta P(\vec{r}, t) = C [I_3 + r \cos(\gamma) I_4],$$

where,

$$I_3 = \int_{-r \cos(\gamma)}^{a - r \cos(\gamma)} \frac{u}{(u^2 + r^2 \sin^2(\gamma))^{\frac{3}{2}}} du = \frac{1}{r} - \frac{1}{(r^2 + a^2 - 2ar \cos(\gamma))^{\frac{1}{2}}},$$

and

$$I_4 = \int_{-r \cos(\gamma)}^{a - r \cos(\gamma)} \frac{1}{(u^2 + r^2 \sin^2(\gamma))^{\frac{3}{2}}} du = \frac{1}{r^2 \sin^2(\gamma)} \left(\cos(\gamma) + \frac{a - r \cos(\gamma)}{(r^2 + a^2 - 2ar \cos(\gamma))^{\frac{1}{2}}} \right).$$

Therefore,

$$\begin{aligned} \Delta P(\vec{r}, t) &= C \left[\frac{1}{r} - \frac{1}{(r^2 + a^2 - 2ar \cos(\gamma))^{\frac{1}{2}}} + \frac{\cos^2(\gamma)}{r \sin^2(\gamma)} + \frac{\cos(\gamma)}{r \sin^2(\gamma)} \frac{(a - r \cos(\gamma))}{(r^2 + a^2 - 2ar \cos(\gamma))^{\frac{1}{2}}} \right] \\ \Delta P(\vec{r}, t) &= C \csc^2(\gamma) \left[\frac{1}{r} - \frac{1 - \frac{a}{r} \cos(\gamma)}{(r^2 + a^2 - 2ar \cos(\gamma))^{\frac{1}{2}}} \right] \end{aligned} \quad (3.40)$$

The gives the acoustic signal from the engine at each observation point at time t. Each engine will have a different location and a different phase angle.

Using the index “*i*” to denote each engine, the sound level measured at the BPF at each field point is proportional to,

$$\overline{\left| \sum_{i=1}^4 P_i(\vec{r}, t) \right|^2} = \frac{1}{T} \int_0^T \left| \sum_{i=1}^4 P_i(\vec{r}, t) \right|^2 dt \quad (3.41)$$

In the same manner as Models A and B, MathCAD was utilized to manipulate the arrays and generate values for the acoustic intensity for each observation point. Plots of the

model results at the phase angle sets defined in the experimental section are shown in Figures 3.8-3.10.

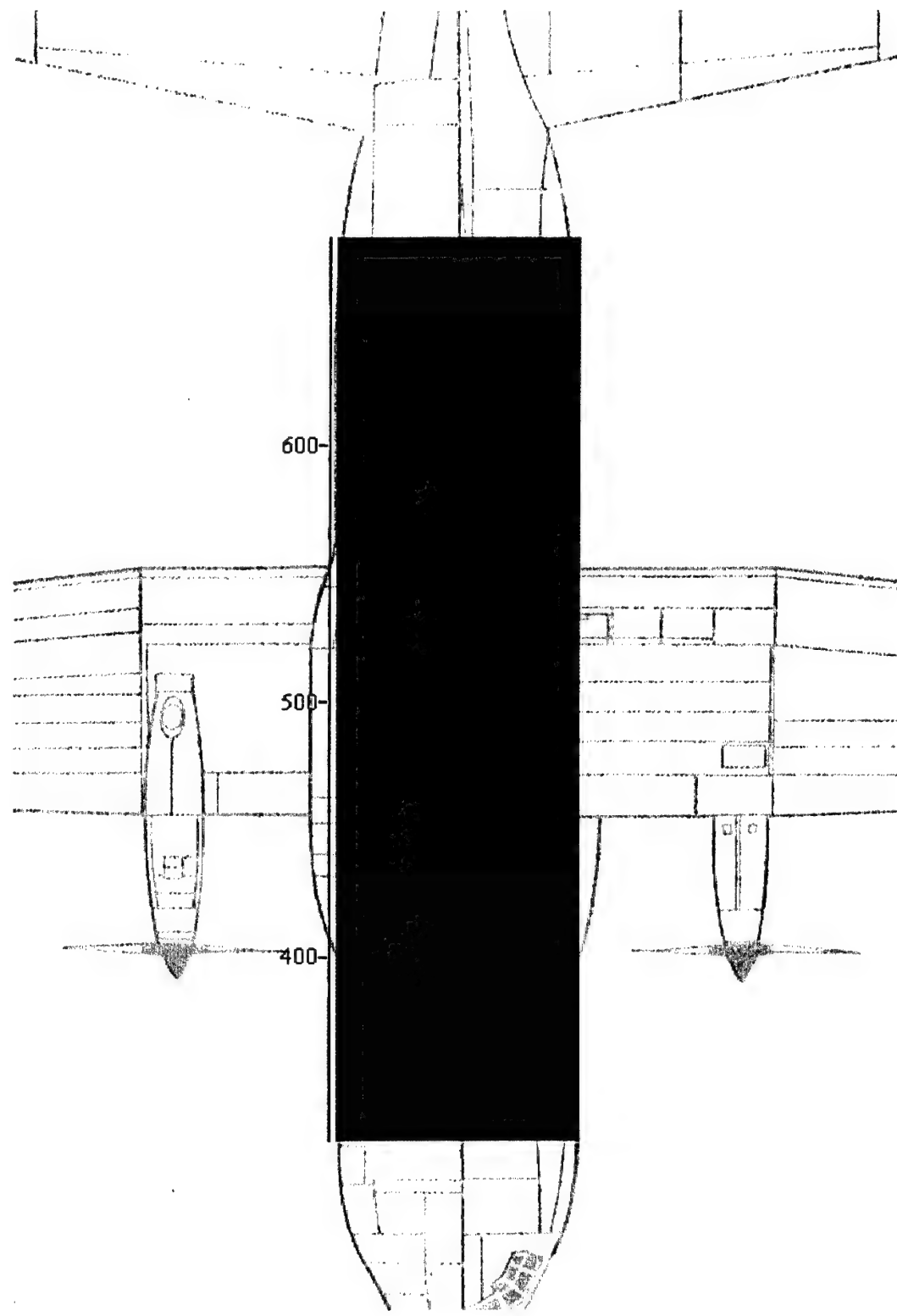


Figure 3.8.. Predicted Fuselage Acoustic Intensity - Model C - Phase Angle (180°, 180°, 180°, 180°).

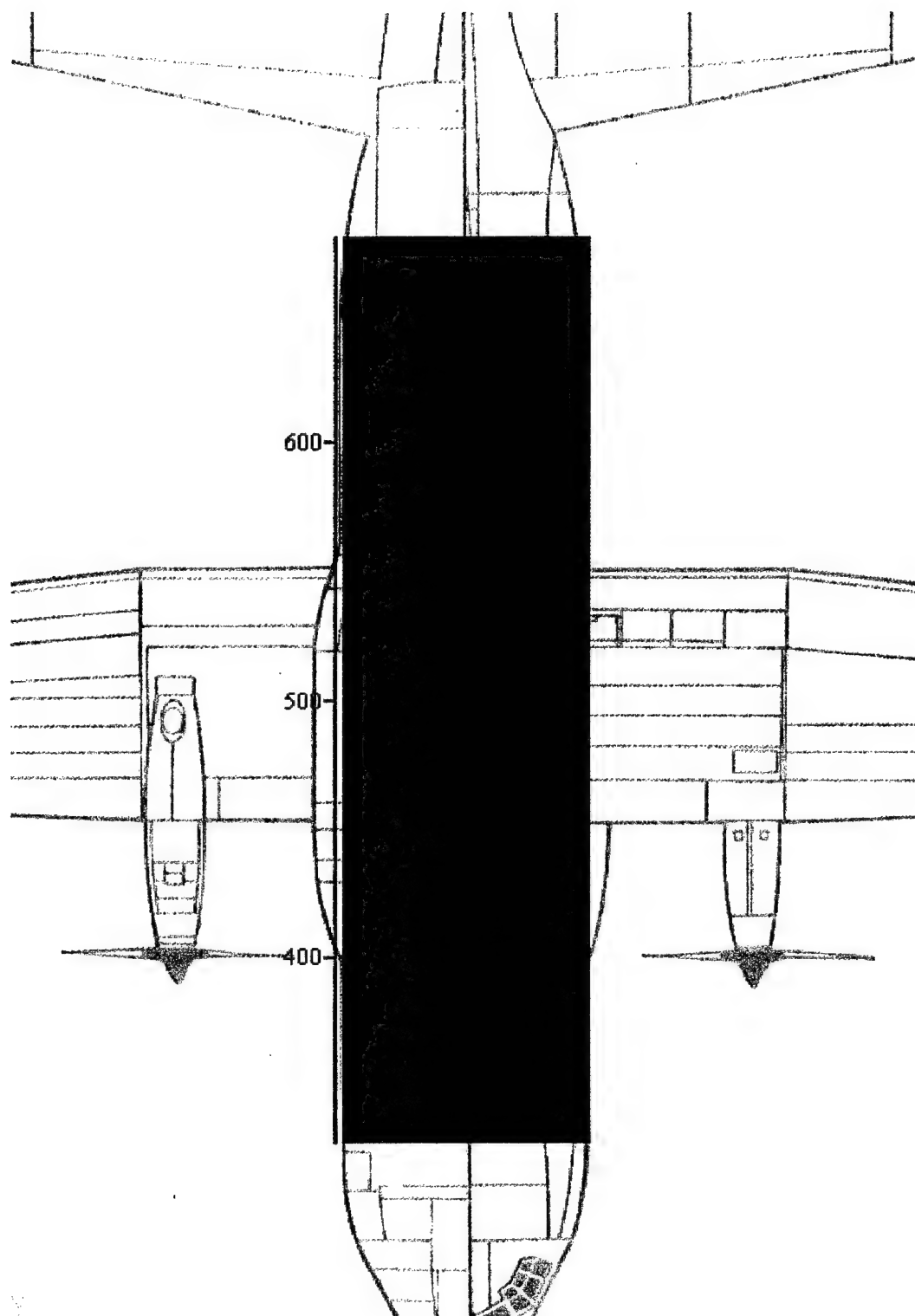


Figure 3.9. Predicted Fuselage Acoustic Intensity - Model C - Phase Angle (120°, 150°, 180°, 150°)

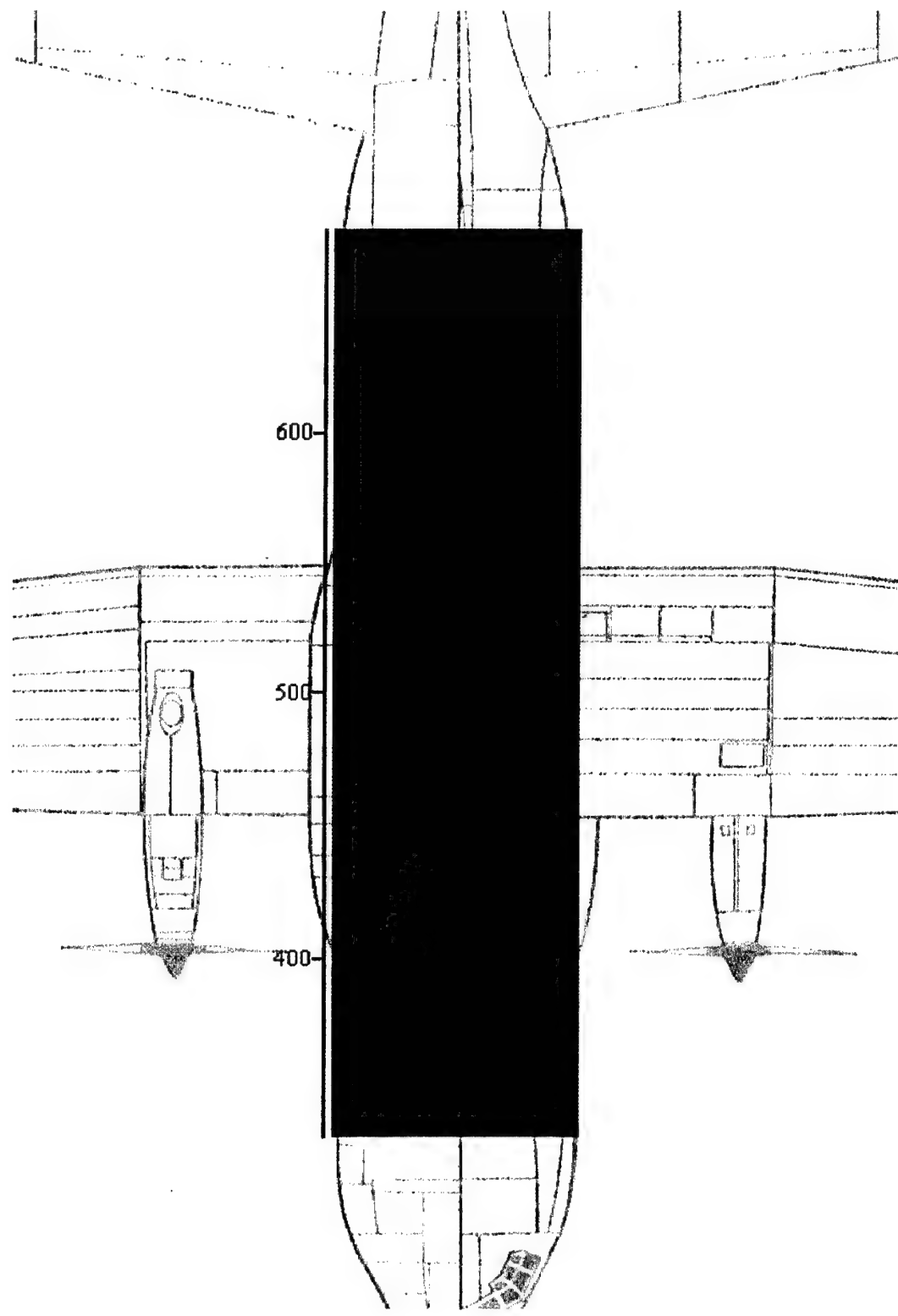


Figure 3.1011. Predicted Fuselage Acoustic Intensity - Model C - Phase Angle (120°, 150°, 180°, 180°)

Section 4 - DISCUSSION AND CONCLUSIONS

Model A appears to exhibit a couple of characteristics of the actual data set. Phase angle set 180°, 180°, 180°, 180° (case 1) produced an intensity region in the plane of the propeller. This result correlates well with the actual data except that the observed data has the band shifted slightly aft; a phenomenon that seems largely attributed to the speed of the aircraft. A relative observation point was determined based upon the amount of time required for the wave generated from each source to propagate to the y-coordinate of each observation point. These changes in the path distance corresponded to a wider intensity band that included the region indicated by the observed data. By contrast, comparison of the 120°, 150°, 180°, 180° (case2) and 120°, 150°, 180°, 150° (case3) phase sets did not compare well with the observed data sets. Variations in the relative propeller phase in Model A did not result in the unusual lower intensity zone on the RHS of the aircraft as in Figure 2.7 nor the large cool regions identified in Figure 2.8, only variations in the width of the propeller plane intensity. Model B did not correlate with the actual data to any greater degree than Model A.

Model B generated plots that exhibited a considerable amount of detail. The distributions generated for case 1 match the data set fairly well with the exception that the regions of high acoustic intensity and low acoustic intensity were reversed. The actual data set had higher levels of noise in the BPF near the perimeter of the fuselage, whereas Model B predicted lower noise levels. Analysis of the other two cases did not match up nearly as

well. Modeled results for case 2 and case 3 produced distributions that were fairly similar to each other; an area of low intensity along the RHS of the graph. Model B did not recreate the shift in the low intensity region from the RHS to the LHS of the aircraft, as the phase on engine 1 is incremented by 30 degrees from 150 degrees to 180 degrees nor did it predict rather large region of low intensity exhibited by case 3. Variations in the relative phase between the engines produced noise zone shifts in the z direction , down the fuselage.

Model C performed equally as well as Model A in producing a region of high intensity in the propeller plane when the engines were in phase, which corresponds fairly well to the observed data. However, as in the other two models, variations in propeller phase did not recreate the shift in the noise field. In fact, as the engine #1 cycled from case 2 to case 3 the predicted noise levels actually increased in the propeller plane. Phase changes contributed to lateral shifts in the distributions in the propeller plane.

This thesis developed a framework for determining the acoustic intensity at an observation point based upon Green's Function techniques. Three models were initially considered, a monochromatic point source, an extended pulsating disk, and a uniformly rotating paddle. Although all three exhibited some characteristics of the actual data set, they ultimately failed to adequately predict the shifting in the noise field associated with controlled variations of the relative propeller phase. The actual source function may be a combination of Model B and Model C. i.e.. some sort of extended line source. since Model B produced variations in the z direction and Model C the y direction. Future work

should center on developing more appropriate functions to represent the source and investigate application of these techniques to the far-field noise.

REFERENCES

1. Drendel, Lou C-130 Hercules in Action, Carrollton, TX: Squadron/Signal Publications, Inc., 1984; p 35.
2. "OSHA Logging Advisor, Table G-16 Permissible Noise Exposurers" [3 Sept 2002], Available http://www.osha-slc.gov/SLTC/logging_advisor/1910_0095.html.
3. Ohlin, Doug. "Cost Effectiveness of Hearing Conservation Programs" US Army Center for Health Promotion and Preventive Medicine, [1 Sept 2002], Available <http://chppm-www.apgea.army.mil/hcp/costeffective/aspx>.
4. Willis, Conrad M., W. H. Mayes, and E. F. Daniels, "Effects of Propeller Rotation Direction on Airplane Interior Noise Levels," National Aeronautics and Space Administration, Scientific and Technical Information Branch, Langley Research Center, Hampton, Virginia, NASA Technical Paper 2444, July 1985; p 1.
5. Grewal, A., L. Pavel, D.G. Zimcik, B. Leigh, and W. Xu, "Application of Feedforward and Feedback Structural Control for Aircraft Cabin Noise Reduction," in Journal of Aircraft, vol 38, no. 4, Feb. 1991, pp 164-173.
6. Hansen, Colin H. Understanding Active Noise Cancellation, London: Spon Press, 2001; p 1.
7. Hansen; p 128.
8. Sollo, Antonio, L. Lecce, V. Quaranta, N. Doelman, and E. Doppenberg, "Active Noise Control on ATR Fuselage Mock-Up By Piezoceramic Actuators," in AIAA/CEAS Aeroacoustics Conference, 4th (19th AIAA AEROACoustics Conference), Toulouse, France, June 2-4, 1998, Collection of Technical Papers. Pt. 1 (A98-30801 07-71), Reston, VA, American Institute of Aeronautics and Astronautics, 1998; pp 174-175.
9. Pla, F., G. Goodman, R. Ranaudo, and R. Silcox, "Cabin Noise Cancellation Using Active RPM Control- OV-10A Flight Test Results," GE Corporate Research and Development, Schenectady, NY, NASA Lewis, Cleveland, OH, and NASA Langley, Hampton, VA, Prepared for the 15th AIAA Aeroacoustics Conference, Long Beach, California, October 25-27, 1993, AIAA 93-4438; p 1.

REFERENCES (Continued)

10. "Facts on the Mighty Hercules" [5 September 2002] Available, http://www.c130.robins.af.mil/Herc_Facts/hercinfo.htm.
11. "Synchrophaser System" [16 June 1998] Available, [heep://www.Hamilton-standard.com/vpv/dir1/propsync.htm](http://www.Hamilton-standard.com/vpv/dir1/propsync.htm).
12. Kinsler, Lawrence E, A. R. Frey, A. B. Coppens, and J. V. Sanders Fundamentals of Acoustics, 4th ed., New York: John Wiley & Sons, Inc., 2000; p142.
13. Jackson, J.D. Classical Electrodynamics, 2nd ed., New York: John Wiley & Sons, Inc., 1975; pp 223-226.
14. Jackson; p 225.
15. Jackson; p 392.